# HIGH-SENSITIVITY 86 GHz (3.5 mm) VLBI OBSERVATIONS OF M87: DEEP IMAGING OF THE JET BASE AT A RESOLUTION OF 10 SCHWARZSCHILD RADII

Kazuhiro Hada[1,2], Motoki Kino[3], Akihiro Doi[4], Hiroshi Nagai[5], Mareki Honma[1,6], Kazunori Akiyama[1,7], Fumie Tazaki[1], Rocco Lico[2,8], Marcello Giroletti[2], Gabriele Giovannini[2,8], Monica Orienti[2], and Yoshiaki Hagiwara[1,9]

[1] Mizusawa VLBI Observatory, National Astronomical Observatory of Japan, Osawa, Mitaka, Tokyo 181-8588, Japan; kazuhiro.hada@nao.ac.jp
[2] INAF Istituto di Radioastronomia, via Gobetti 101, I-40129 Bologna, Italy
[3] Korea Astronomy and Space Science Institute (KASI), 776 Daedeokdae-ro, Yuseong-gu, Daejeon 305-348, Korea
[4] Institute of Space and Astronautical Science, Japan Aerospace Exploration Agency, 3-1-1 Yoshinodai, Chuo, Sagamihara 252-5210, Japan
[5] National Astronomical Observatory of Japan, Osawa, Mitaka, Tokyo 181-8588, Japan
[6] Department of Astronomical Science, The Graduate University for Advanced Studies (SOKENDAI), 2-21-1 Osawa, Mitaka, Tokyo 181-8588, Japan
[7] Department of Astronomy, Graduate School of Science, The University of Tokyo, 7-3-1 Hongo, Bunkyo-ku, Tokyo 113-0033, Japan
[8] Dipartimento di Fisica e Astronomia, Università di Bologna, via Ranzani 1, I-40127 Bologna, Italy
[9] Toyo University, 5-28-20 Hakusan, Bunkyo-ku, Tokyo 112-8606, Japan

## ABSTRACT

We report on results from new high-sensitivity, high-resolution 86 GHz (3.5 mm) observations of the jet base in the nearby radio galaxy M87, obtained by the Very Long Baseline Array in conjunction with the Green Bank Telescope. The resulting image has a dynamic range exceeding 1500 to 1, the highest ever achieved for this jet at this frequency, resolving and imaging a detailed jet formation/collimation structure down to ~10 Schwarzschild radii ($R_s$). The obtained 86 GHz image clearly confirms some important jet features known at lower frequencies, i.e., a jet base with a wide opening angle, a limb-brightened intensity profile, a parabola-shape collimation profile and a counter jet. The limb-brightened structure is already well developed at <0.2 mas (<28 $R_s$, projected) from the core, where the corresponding apparent opening angle becomes as wide as ~100°. The subsequent jet collimation near the black hole evolves in a complicated manner; there is a "constricted" structure at tens of $R_s$ from the core, where the jet cross section is locally shrinking. We suggest that external pressure support from the inner part of the radiatively inefficient accretion flow may be dynamically important in shaping/confining the footprint of the magnetized jet. We also present the first 86 GHz polarimetric experiment using very long baseline interferometry for this source, where a highly polarized (~20%) feature is detected near the jet base, indicating the presence of a well-ordered magnetic field. As a by-product, we additionally report a 43/86 GHz polarimetric result for our calibrator 3C 273, suggesting an extreme rotation measure near the core.

*Key words:* galaxies: active – galaxies: individual (M87) – galaxies: jets – radio continuum: galaxies

## 1. INTRODUCTION

Accreting supermassive black holes at the center of active galaxies produce powerful relativistic jets that are observed as a collimated beam of plasma, often propagating beyond the host galaxies. Understanding the formation, collimation, and propagation of relativistic jets is a longstanding concern in astrophysics (Blandford & Rees 1974; Blandford & Znajek 1977; Blandford & Payne 1982; Begelman et al. 1984), and recent theoretical progress based on general relativistic magnetohydrodynamical simulations has begun to elucidate the roles of the central black hole, surrounding accretion flow, and magnetic fields threading them, as well as the mutual interactions among these components, in generating and collimating a jet (e.g., McKinney 2006; Komissarov et al. 2007; McKinney & Blandford 2009; Tchekhovskoy et al. 2011; McKinney et al. 2012). To test the implications from such theories and then to better understand the jet formation, it is necessary to present a detailed observation that can image the relevant scales.

M87 was the first extragalactic jet to be discovered, by Curtis nearly 100 years ago (Curtis 1918). This jet is exceptionally close to us (D = 16.7 Mpc; Blakeslee et al. 2009), and is bright across the entire electromagnetic spectrum from radio to TeV γ-rays. These observational advantages have allowed a broad range of studies associated with the physics of relativistic jets, including the large-scale jet morphology (e.g., Owen et al. 1989), the nature

of the optical jet emission and shocks (e.g., Biretta et al. 1999; Perlman et al. 2001), and the origin of the high-energy X-ray to γ-ray emission (e.g., Harris et al. 2006; Abramowski et al. 2012; Hada et al. 2014). Moreover, optical measurements of the nuclear stellar dynamics suggest the presence of a huge central black hole of $M_{BH} = (6–6.6) \times 10^9 M_\odot$ (Gebhardt & Thomas 2009; Gebhardt et al. 2011), although gas-dynamical measurements imply a value for $M_{BH}$ a factor of two smaller (Ford et al. 1994; Harms et al. 1994; Macchetto et al. 1997; Walsh et al. 2013). The combination of the proximity and the large black hole yields a linear resolution down to 1 milliarcsecond (mas) = 0.08 pc = 140 Schwarzschild radii ($R_s$) (for D = 16.7 Mpc and $M_{BH} = 6 \times 10^9 M_\odot$), which is typically 10 to 100 times finer than those accessible in distant quasars or blazars. Therefore, M87 offers a privileged opportunity for probing the launch/formation scales of a relativistic jet with high-resolution observations using very long baseline interferometry (VLBI).

With the recent advent of the global short-millimeter VLBI project, known as the Event Horizon Telescope (EHT), observational studies of the M87 jet have become possible at a spatial scale comparable to the event horizon. At 1.3 mm (a frequency of 230 GHz) Doeleman et al. (2012) resolved a jet base/launching structure that has a size of 40 µas, corresponding to 5.5 $R_s$ (if $M_{BH} = 6.4 \times 10^9 M_\odot$ is adopted). More recently, interferometric closure phases for the corresponding

structure have been obtained at this wavelength (Akiyama et al. 2015), allowing a comparison between the observation and some horizon-scale theoretical models. Going to shorter wavelengths is also beneficial with respect to the synchrotron opacity, since the jet base becomes more transparent to the self-absorption effect (Königl 1981). Indeed, the $\lambda^{+0.94}$ dependence of the position of the M87 radio core revealed by astrometric measurements suggests the 1.3 mm core to be located within a few $R_s$ of the black hole (Hada et al. 2011). Nevertheless, it is still technically challenging to synthesize interferometric images from current VLBI experiments at such short wavelengths due to the limited number of available antennas (thus only sparse *uv*-coverage) as well as the severe atmospheric disturbance (thus shorter coherence time). This prevents us from tracking the larger-scale propagation of the flow launched from the central horizon-scale dimension, which is essential to fully understand the subsequent acceleration and collimation of the jet.

So far, VLBI imaging studies of M87 have mostly been made at 7 mm (43 GHz), 1 cm (22–24 GHz), 2 cm (15 GHz), or longer. In these bands the M87 jet is bright enough and a sufficient number of VLBI stations are available to allow adequate *uv*-coverage. Previous high-quality VLBI images of the M87 inner jet revealed some important features such as a base with wide opening angle, a limb-brightened intensity profile, and a counter jet (Junor et al. 1999; Ly et al. 2004, 2007; Kovalev et al. 2007; Hada et al. 2011), as well as a detailed movie near the jet base (Walker et al. 2008). More recently, the inner jet was found to sustain a parabola-shape collimation profile over a wide range of distance from ∼100 to ∼$10^5 R_s$ from the nucleus (Asada & Nakamura 2012; Hada et al. 2013; Nakamura & Asada 2013). However, in these bands, it is impossible to achieve angular resolution comparable to that of the short-millimeter VLBI unless relying on a space-VLBI satellite (Hirabayashi et al. 1998; Dodson et al. 2012; Kardashev et al. 2013). In addition, the higher optical depth at such long wavelengths precludes us from observing the close vicinity of the black hole. As a result, there still remains a large gap in our current understanding of this jet between the centimeter and the short-millimeter VLBI scales.

In this context, an important "bridge" to connect this gap is observational study at 3.5 mm (86 GHz). At present, 3.5 mm is the shortest wavelength where one can reliably obtain synthesized VLBI images, as represented by studies with the Global Millimeter VLBI Array (GMVA; e.g., Agudo et al. 2007; Giroletti et al. 2008; Lee et al. 2008; Molina et al. 2014; Hodgson et al. 2015; Koyama et al. 2015). The angular resolution with 3.5 mm VLBI is typically twice as good as that at 7 mm, and the transparency to a jet base is also higher. On the other hand, compared to 1.3 mm, one can detect the extended (optically thin) emission much further down the jet due to the steep-spectral nature of the synchrotron radiation, which allows a better monitoring of the larger-scale jet propagation. Therefore, the use of 3.5 mm is currently an optimal choice in terms of angular resolution, opacity, and capability for imaging a jet. Nevertheless, there have still been fewer M87 observations in this band because 3.5 mm VLBI is generally less sensitive than that at 7 mm due to the more rapid atmospheric fluctuations as well as the worse effective aperture efficiency of telescopes. Thus the brightness of the M87 jet base (typically hundreds of mJy to <1 Jy) may not be sufficient to detect interferometric fringes at high signal-to-noise ratios

(S/Ns). Only a handful of 3.5 mm VLBI images of M87 are published in the literature (Lee et al. 2008; Rioja & Dodson 2011; Nakamura & Asada 2013), and the obtained jet structure is not well characterized since the dynamic ranges of their images are only at a level of ∼100, although 3.5 mm images of somewhat better quality showing a hint of limb-brightening are presented in one of the early GMVA results (Krichbaum et al. 2006).

In this paper we report on results from new high-sensitivity, high-resolution 3.5 mm VLBI observations of the M87 jet, obtained by the Very Long Baseline Array (VLBA) connected to the Green Bank Telescope (GBT). This is the first GBT-incorporated 3.5 mm VLBI observation of M87. The large collecting area of GBT, together with the recent implementation of the National Radio Astronomy Observatory's (NRAO) wideband recording system, has allowed us to obtain an image of the M87 jet of unprecedented quality in this band, where the dynamic range has improved by a factor of greater than 10 from the previous VLBA-only 86 GHz images (Rioja & Dodson 2011; Nakamura & Asada 2013). In the next section we describe our observations and data reduction. In Sections 3 and 4, our new results are presented and discussed, supplementarily using contemporaneous data sets at the lower frequencies. In the final section we will summarize the paper. Throughout the paper we adopt $D = 16.7$ Mpc and $M_{BH} = 6.0 \times 10^9 M_\odot$ for M87, corresponding to 1 mas = 0.08 pc = $140 R_s$. Spectral index $\alpha$ is defined as $S_\nu \propto \nu^{+\alpha}$. Also, any $\lambda$-related numbers are described in frequency units in the rest of the paper.

## 2. OBSERVATIONS AND DATA REDUCTION

### 2.1. 86 GHz Data

In 2014 February we observed M87 at 86 GHz with VLBA in conjunction with GBT. From VLBA eight out of the ten stations participated in this program since the other two (i.e., Hancock and Saint Croix) do not have an 86 GHz receiver. To increase the overall sensitivity, we made an 8 hr long quasi-full-track observation twice on February 11 and 26. The observations were made in dual (left/right-hand circular) polarization mode. The received signals were sampled with 2-bit quantization and recorded at an aggregate rate of 2 Gbps (a total bandwidth of 512 MHz) using the digital-down-converter-4 (DDC-4) wideband recording mode. The down-converted signals were divided into two 128 MHz sub-bands in each polarization. As an overall system calibrator (fringe check, bandpass, delay tracking, see below) of this program, we inserted 5 minute scans on the nearby bright source 3C 273 (10° apart from M87 on the sky) every 30 minutes. 3C 273 was observed also for the purpose of antenna-pointing by adding scans of 6 minutes duration every 30–60 minutes. The second epoch had better weather conditions and system temperatures over the array. The information on these data is summarized in Table 1.

The initial data calibration was performed with the Astronomical Image Processing System (AIPS) developed at NRAO. We first corrected the visibility amplitude by applying the measured system noise temperature and the elevation–gain curve of each antenna. Atmospheric opacity corrections were made by solving for receiver temperature and zenith opacity for each antenna. We then calibrated the amplitude part of the

**Table 1**
VLBA Observations of M87

| UT Date | $\nu$ (GHz) (a) | Stations (b) | $\Delta\nu$ (MHz) (c) | Beam Size (mas × mas, deg) (d) | $I_{\rm peak}$ $\left(\dfrac{\rm mJy}{\rm beam}\right)$ (e) | $I_{\rm rms}$ $\left(\dfrac{\rm mJy}{\rm beam}\right)$ (f) | $I_{\rm peak}/I_{\rm rms}$ (g) |
|---|---|---|---|---|---|---|---|
| 2014 Feb 11 | 86.266 | VLBA, GBT, −SC, −HN | 512 | 0.50 × 0.11, −12 (0.42 × 0.08, −13) | 549 | 0.63 | 871 |
| 2014 Feb 26 | 86.266 | VLBA, GBT, −SC, −HN | 512 | 0.30 × 0.10, −10 (0.26 × 0.08, −11) | 521 | 0.36 | 1447 |
| 2014 Feb (11+26)[h] | 86.266 | VLBA, GBT, −SC, −HN | 512 | 0.38 × 0.11, −10 (0.28 × 0.08, −12) | 547 | 0.29 | 1886 |
| 2014 Mar 8 | 43.230 | VLBA, −MK, −FD | 128 | 0.58 × 0.26, 25 (0.50 × 0.21, 27) | 786 | 0.85 | 924 |
|  | 23.830 | VLBA, −MK, −FD | 128 | 0.94 × 0.48, 18 (0.84 × 0.39, 21) | 880 | 0.82 | 1073 |
| 2014 Mar 26 | 43.296 | VLBA | 256 | 0.43 × 0.21, 12 (0.35 × 0.17, 12) | 795 | 0.50 | 1590 |
|  | 23.894 | VLBA | 256 | 0.70 × 0.37, 1 (0.60 × 0.30, −1) | 926 | 0.43 | 2153 |
| 2014 May 8 | 43.296 | VLBA | 256 | 0.40 × 0.21, −2 (0.31 × 0.16, −3) | 735 | 0.56 | 1312 |
|  | 23.894 | VLBA | 256 | 0.69 × 0.36, −6 (0.59 × 0.29, −7) | 869 | 0.64 | 1358 |

**Note.** (a) Central frequency. (b) Participating stations. VLBA indicates all ten VLBA stations. GBT, SC, HN, MK and FD are the Green Bank Telescope, Saint Croix, Hancock, Mauna Kea and Fort Davis, respectively. A minus sign before a station name means the absence of that station. (c) Total bandwidth. (d) Synthesized beam with a natural weighting scheme. For reference, a beam size with a uniform weighting scheme is also shown in brackets. (e) Peak intensity of M87 images with a natural weighting scheme. (f) Off-source rms image noise level of M87 images under a natural weighting scheme. (g) Dynamic range calculated with $I_{\rm peak}$ and $I_{\rm rms}$. (h) Combined visibility data over the two epochs.

bandpass characteristics for each station using the autocorrelation spectra of 3C 273.

The calibration of the visibility phase was made following the amplitude calibration. To recover 86 GHz fringes as much as possible, we performed the phase calibration in the following way. We first corrected known phase variations due to parallactic angle effects. Next, the instrumental phase and delay offsets for each antenna were derived using a scan of 3C 273, and subtracted from the whole data set assuming that they are constant with time (note that at 86 GHz no pulse-cal signals are available to calibrate instrumental effects). After that, we ran a global fringe-fitting on 3C 273 with its source structure model created by the procedure described below (a point source model was assumed in the first round where the source model was not available), and derived time evolutions of the residual delay, rate, and phase for each intermediate frequency (IF) separately. We detected fringes for most of the scans at adequate S/Ns. Since the derived residual delay component (which mainly comes from unpredicted atmospheric fluctuations in the correlation stage) varies slowly on the sky, we can use the solutions of 3C 273's delay as a good first-order approximation for those of M87's residual delay. We thus interpolated the derived delay solutions of 3C 273 to the scans of M87. Implementing this process, we can now proceed to fringe-fitting on M87 with a tight delay search window (as small as ±10 ns), which is quite effective in avoiding false signals. We performed a global fringe-fitting on M87 with a solution interval of 15 s and an S/N threshold of 4.0. Since the phase and delay offsets between IFs are already removed, we derived IF-averaged solutions for M87 to increase S/N by a factor of 1.4. Similarly to 3C 273, we ran two cycles of fringe-fitting iteratively; the first round (where no source model was available) was performed with a point source model, and after creating a coarse image, the second round was executed with the source model. This indeed slightly increased the fringe detection rate. In every fringe-fitting the most sensitive station, GBT, was used as the reference antenna.

Through this procedure, we recovered a number of fringes at sufficient S/Ns. In Figure 1 we show (normalized) histograms of S/N for the detected fringes on M87 and 3C 273. For 3C 273 the median/mean S/Ns were 38 and 38, respectively.
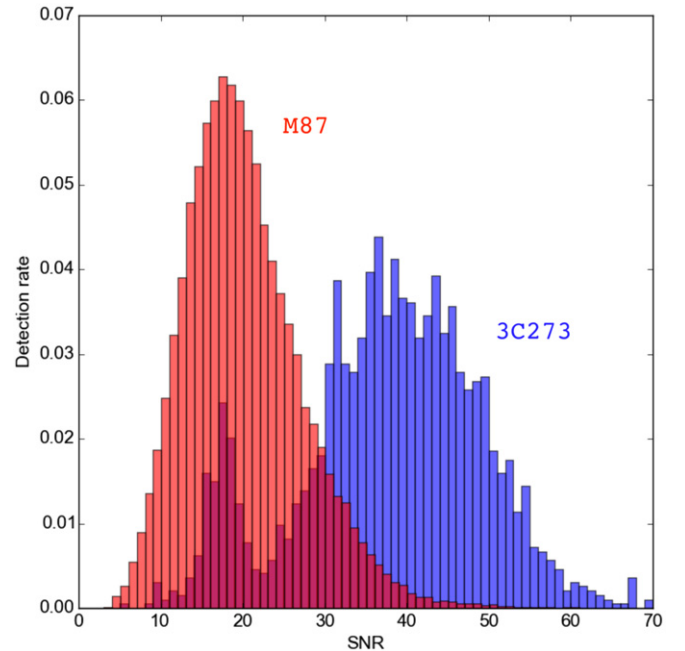


**Figure 1.** Normalized histograms of signal-to-noise ratio for the detected fringes (by global fringe-fitting). The red histogram is for M87 and the blue one for 3C 273. A solution interval of 15 s is used here.

For M87 the median/mean S/Ns were 19 and 20, respectively. Note that the S/N histogram for 3C 273 is relatively widely distributed. This is because the source structure of 3C 273 is highly complicated (see the Appendix) and the correlated flux density changes more drastically with baseline length than in the case of M87.

After the visibility data became coherent with time and frequency, the data were integrated over frequency (but the two IFs kept separated), and in time to 30 s. These data were then used for creating images.

We performed our imaging process in the following way. We first exported the averaged data to the Difmap software (Shepherd et al. 1994) and performed intensive flagging of the visibility data. Antenna pointing is generally less
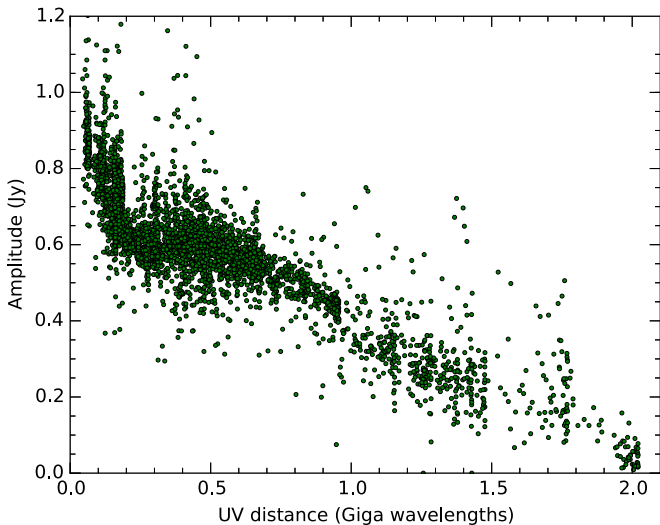
**Figure 2.** Visibility amplitude vs. *uv*-distance plot of M87 for the VLBA +GBT 86 GHz observations. The visibility data are shown after self-calibration.

accurate at 86 GHz than at lower frequencies, and this causes an unwanted systematic decrease of visibility amplitude in some scans. These scans then cause significant sidelobes in the initial stage of the imaging process, which prevents us from reconstructing a reliable CLEAN/deconvolution model. Thus, in addition to obvious outliers, we carefully flagged such bad scans in an antenna-based manner.

Following the initial exhaustive flagging, we then worked on iterative CLEAN/self-calibration processing. We conducted this process using Difmap and AIPS in a hybrid manner. We used Difmap only to perform CLEAN deconvolution (because CLEAN with Difmap is faster and more intuitive than with AIPS). Then after obtaining a reasonable set of CLEAN components, the model and the (uncalibrated) visibility data were exported back to AIPS, and we performed self-calibration using the AIPS task CALIB. This is advantageous for better calibration because the self-calibration with CALIB can be handled more robustly and flexibly (e.g., in terms of weighting for each antenna and S/N cutoff setting) than that in Difmap. Self-calibration with CALIB was also necessary for proper polarization analysis (see below) since CALIB can solve the complex gain terms for LL/RR polarization separately, while Difmap cannot do that. Then the self-calibrated visibility data were again exported back to Difmap to create an improved CLEAN model. We repeated this CLEAN/self-calibration round until the reconstructed CLEAN model no longer improved significantly. In the first several CLEAN/self-calibration cycles, the phase-only self-calibration was done, and after the phase part was well corrected; the visibility amplitude was also self-calibrated iteratively with solution intervals starting from several hours down to a few minutes.

In Figure 2 we show a resulting *uv*-distance plot of the calibrated visibility amplitude of M87. Thanks to the excellent quality of the data set, one can see that the visibilities are homogeneously sampled over the entire *uv*-distance and thus the overall trend is well defined. One can see that the whole visibility set primarily consists of two components. One is an extended component that contributes significantly at baselines shorter than $\lesssim 0.2$ G$\lambda$, while the other is a compact component that dominates beyond 0.2 G$\lambda$ to the longest 2 G$\lambda$ baseline. For

the compact component, the correlated flux densities are monotonically decreasing with increasing *uv*-distance, and the amplitude is $\lesssim 100$ mJy at the longest baseline. Despite such low flux densities, the signals were robustly detected since the longest baseline consists of the GBT–MK pair.

### 2.2. Polarization Analysis at 86 GHz

Although our 86 GHz observations were not ideally designed for accurate polarimetric study, we can still attempt a polarization analysis by taking advantage of the scans of 3C 273. Following the parallactic angle corrections described above, the cross-hand R–L phase and delay offsets were calibrated using a scan of 3C 273. The feed polarization leakage for each antenna was corrected by using the LPCAL method in AIPS (Leppänen et al. 1995) with a total intensity model of 3C 273. The derived leakage values varied with station, polarization, IF, and epoch, but we obtained a value of $(9 \pm 2)\%$ when averaged over the whole array, which is consistent with the values derived in other VLBA 86 GHz polarimetric studies (e.g., $(6 \pm 3)\%$; Martí-Vidal et al. 2012). This is somewhat larger than typical leakages obtained at lower frequencies, and roughly close to the upper end where the linear approximation ("*D*-term") scheme is validated. GBT was one of the best stations, where the leakages were as small as $\sim 5\%$, while a few of the other stations (particularly North Liberty and Brewster) occasionally showed leakages up to $\sim 20\%$. For each antenna we confirmed an overall consistency (within a few per cent) on the derived leakages over the different IFs and epochs, indicating that the calibration is reasonably valid. Following the prescription in Roberts et al. (1994), we estimate that the corresponding error in fractional polarization in our images is $\sim 1\%$. As a check, we examined the minimum detectable polarization by using our 3C 273 polarization map, and confirmed that a fractional polarization down to $\sim 0.7\%$ was recovered at $3\sigma$ in the core region (see the Appendix). This is consistent with the above calculation.

Regarding the electric vector polarization angle (EVPA), we cannot derive its absolute value from our data alone, since we did not perform any additional EVPA-calibration observation. However, we found a 43 GHz VLBA observation of 3C 273 that was carried out close in time with ours (on 2014 February 25) in the Boston University blazar monitoring program. We used this 43 GHz polarization image as a reference for our EVPA correction (see Figure 11 in the Appendix). Here we assume that the EVPA of the outermost polarized component (P3 at 1.5 mas from the core) is stable in both time and frequency, and we performed a nominal correction of EVPA by matching the observed 86 GHz EVPA of P3 to the 43 GHz one. Note that this assumption may not be correct, since the previous concurrent 86/43 GHz VLBA polarimetric study of this source suggests a large rotation measure (RM) of $\sim 2 \times 10^4$ rad m$^{-2}$ for inner jet components at $\sim 0.8$ mas from the core (see Attridge et al. 2005). In fact, a comparison of the present 86/43 GHz polarization images similarly implies a significant RM of the order of $\sim 4 \times 10^3$ rad m$^{-2}$ around P3 (see the Appendix for more details). If this is the case, one would expect another systematic rotation of the 86 GHz EVPA by about $\sim 8°$ with respect to that at 43 GHz (i.e., $\Delta\chi_{\mathrm{RM}} \sim 8°$). As for the Boston 43 GHz polarization image, we adopt its EVPA uncertainty to be $\Delta\chi_{43\,\mathrm{GHz}} \sim 10°$ based on Jorstad et al. (2005). Therefore, we estimate that a potential total uncertainty of absolute EVPA in our 3C 273 86 GHz images is
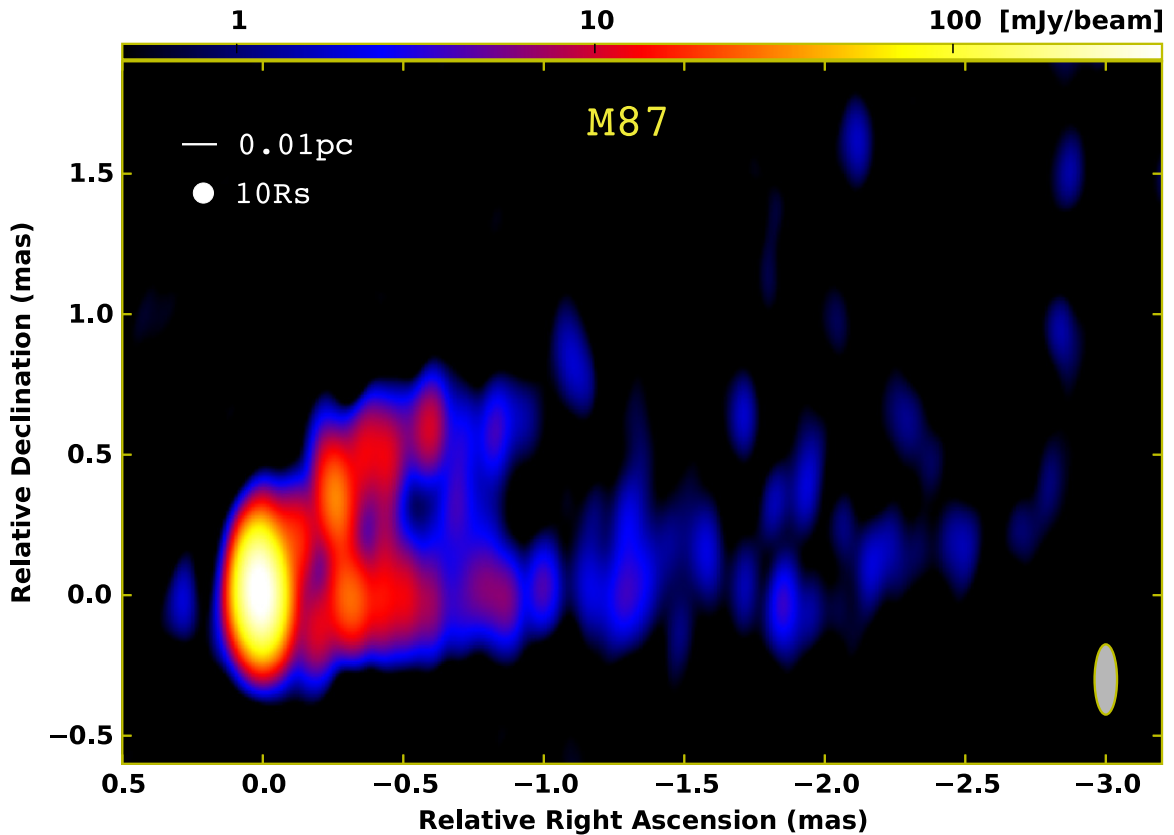
**Figure 3.** VLBA+GBT 86 GHz false-color total intensity image of the M87 jet. The image is produced by combining the visibility data over the two epochs on 2014 February 11 and 26. The restoring beam (0.25 mas × 0.08 mas at PA 0°) is shown in the bottom-right corner of the image. The peak intensity is 500 mJy beam$^{-1}$ and the off-source rms noise level is 0.28 mJy beam$^{-1}$, where the resulting dynamic range is greater than 1500 to 1.

$\Delta\chi_{3C273} \sim \Delta\chi_{43\,GHz} + \Delta\chi_{RM} \sim \pm18°$. Regarding M87, its EVPA uncertainty in 86 GHz images would be somewhat larger than this value, since the lower S/N of polarization signals (S/N ∼ 4.5; see Section 3.4) from this source gives another non-negligible thermal error term. This can be estimated as $\Delta\chi_{therm}$ (radian) $\sim \sigma_p/2P$ where $\sigma_p$ and $P$ are rms noise level and polarized intensity in the polarization map (e.g., Roberts et al. 1994). With S/N = $P/\sigma_p \sim 4.5$, we obtain $\Delta\chi_{therm,M87} \sim 6°$. Assuming that $\Delta\chi_{3C273}$ and $\Delta\chi_{therm,M87}$ are statistically independent, we estimate a total error budget for M87 to be $\Delta\chi_{M87} \sim \pm20°$.

### 2.3. Lower-frequency Data

As supplementary data sets, we additionally made VLBA-only observations of M87 at 24 and 43 GHz close in time with the 86 GHz sessions. The observations were carried out on 2014 March 8, 26, and May 8, where both 24 and 43 GHz were used quasi-simultaneously by alternating the receivers quickly. On March 26 and May 8, all the VLBA stations were present, while on March 8 the antennas at Mauna Kea and Fort Davis were absent. We received only RR polarization signals with a total bandwidth of 128 MHz (on March 8) or 256 MHz (on March 26 and May 8). Among these sessions, the data on March 26 were the best in overall quality, while the data on March 8 were relatively poor. The initial data calibration (a priori amplitude correction, fringe-fitting, and bandpass) was made in AIPS, and the subsequent image reconstruction was performed in Difmap based on the usual CLEAN/self-

calibration procedure. The basic information of these data is also tabulated in Table 1.

### 3. RESULTS

#### 3.1. New 86 GHz Images

In Figure 3 we show a representative 86 GHz image of the M87 jet obtained by our VLBA+GBT observations. For a better visualization, the image is produced by combining the visibility data over the two epochs, and restored with a convolving beam of 0.25 mas × 0.08 mas at a position angle (PA) of 0°. A contour image with a natural weighting scheme is also displayed in the top panel of Figure 4.

Thanks to the significant improvement in sensitivity, a detailed jet structure was clearly imaged down to the weaker emission regions. The resulting image rms noise of the combined image was ∼0.28 mJy beam$^{-1}$. In this period the extended jet was substantially bright down to ∼1 mas from the core. The weak emission was detected (particularly in the southern limb) down to ∼3 mas from the core at a level of 3$\sigma$, and another ∼1–2 mas at 2$\sigma$. The peak surface brightness of the image was 500 mJy beam$^{-1}$ at this resolution, corresponding to an image dynamic range greater than 1500 to 1 (the detailed value varies slightly as a function of the weighting scheme and convolving beam). This is the highest image dynamic range obtained so far at 86 GHz for this jet, and is quite comparable to typical dynamic ranges in VLBA images at 43 GHz (e.g., Ly et al. 2007). We describe a comparison of our 86 and 43 GHz images in the next subsection.
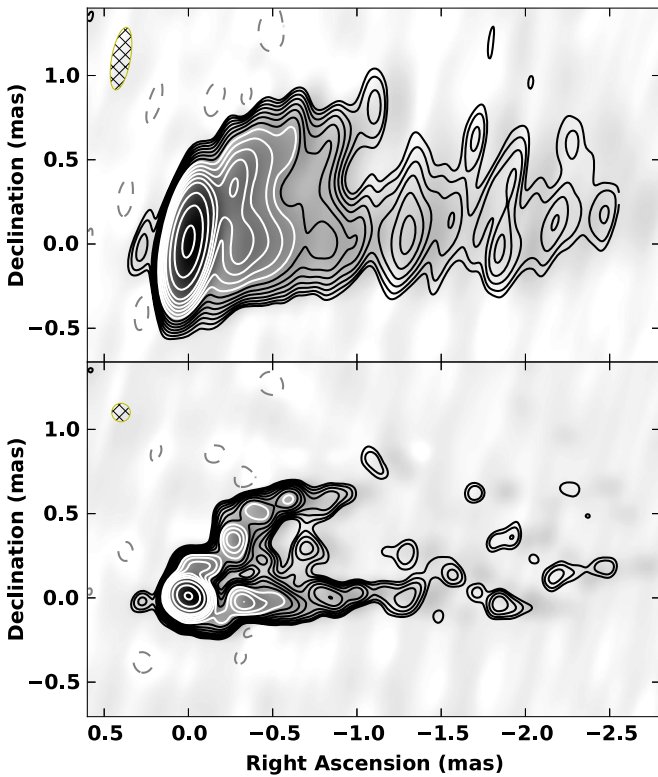
**Figure 4.** VLBA+GBT 86 GHz total intensity contour images of the M87 jet. The upper panel indicates a naturally weighted image with a synthesized beam of 0.37 mas × 0.11 mas at PA −10°. The lower panel shows a better-resolved image restored with a circular Gaussian beam whose FWHM is equivalent to that of the minor axis of the beam used in the top panel. The restored beam is shown at the top-left corner of each panel. Contours in both images are from −1, 1, $2^{1/2}$, 2, $2^{3/2}$, 4... times 0.86 mJy beam$^{-1}$.

**Table 2**
Modelfit Parameters for 86 GHz Core

| Data | $\theta_{maj}$ ($\mu$as) (a) | $\theta_{min}$ ($\mu$as) (b) | PA (deg) (c) | $S_{core}$ (mJy) (d) |
|------|------|------|------|------|
| Feb 11 | 81 ± 4 | 62 ± 10 | 56 ± 9 | 669 ± 67 |
| Feb 26 | 82 ± 3 | 81 ± 7 | 72 ± 20 | 652 ± 65 |
| Feb (11+26)[(e)] | 83 ± 6 | 76 ± 4 | 24 ± 9 | 672 ± 67 |

**Note.** (a) Major axis size of the derived elliptical Gaussians. (b) Minor axis size of the derived elliptical Gaussians. (c) Position angles of the major axes of the Gaussian models. (d) Total flux densities of the Gaussian models. (e) Combined visibility data over the two epochs. For (a)–(c), we estimate a practical uncertainty of each parameter by adopting the difference in the derived results between modelfit in Difmap and JMFIT in AIPS. For (d), we adopt 10% uncertainty based on the absolute accuracy of typical amplitude calibration.

Regarding the individual epochs, the second epoch was better in overall image quality than the first. As listed in Table 1, the synthesized beam for the first epoch is more elongated in the north–south direction than that for the second epoch. This is mainly because the Brewster station, which constitutes the longest baselines in the north–south direction, had higher system noise temperatures during the first session.
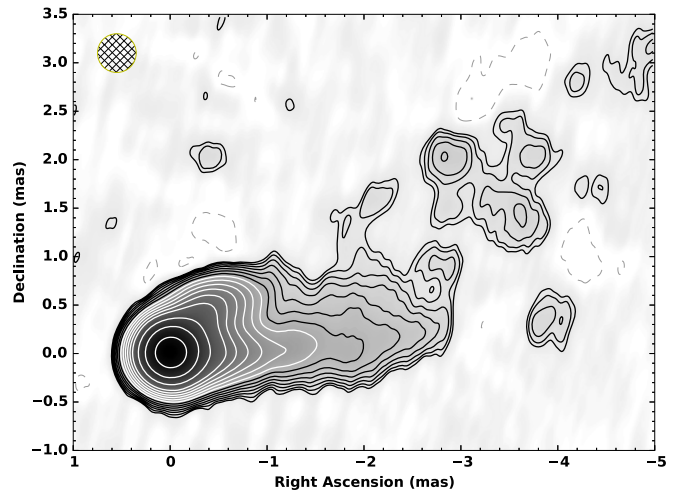


**Figure 5.** Tapered 86 GHz image of the M87 jet. The image is convolved with a circular Gaussian beam of 0.4 mas diameter. The contours are −1, 1, $2^{1/2}$, 2, $2^{3/2}$, 4... times 0.9 mJy beam$^{-1}$.

Thus the less-weighted uv data set on this station creates a slightly larger fringe spacing along the north–south direction.

Consistent with known lower-frequency images, most of the radio emission at 86 GHz is concentrated on the compact radio core at the jet base. To quantify the structure of the core region, we fit the calibrated visibility data with a single elliptical Gaussian model using the Difmap task modelfit. The derived model parameters are summarized in Table 2. As a check we performed the same fitting on the three different data sets, i.e., the February 11 data, the February 26 data, and the combined data, but virtually the same result was obtained. Additionally, we performed another elliptical Gaussian model fitting on the image plane using the AIPS task JMFIT and examined the deconvolved result, but this was also essentially the same within errors. The derived geometry of the core is close to a circular shape with a diameter of ∼80 $\mu$as, which is just between the sizes obtained at 230 GHz (40 $\mu$as; Doeleman et al. 2012) and 43 GHz (110–130 $\mu$as; Hada et al. 2013). A size of 80 $\mu$as is consistent with that obtained in our previous study based on an archival VLBA 86 GHz data set (Hada et al. 2013), but the result presented here is much more reliable. Adopting the parameters derived with the combined data, the brightness temperature of the 86 GHz core is estimated to be $T_B = 1.8 \times 10^{10}$ K. Although the observed epochs are different, this value is quite similar to $T_B$ reported for the 230 GHz core ($(1.2–1.4) \times 10^{10}$ K; Akiyama et al. 2015). No significant valiability was found in $T_B$ of the core between our two 86 GHz sessions.

Downstream of the core, we clearly identified a limb-brightened jet profile as seen in Figures 3 and 4. While such a limb-brightened structure in M87 is repeatedly confirmed in previous VLBA 43 GHz/15 GHz images (e.g., Junor et al. 1999; Kovalev et al. 2007; Ly et al. 2007; Hada et al. 2011, 2013), it was not so clear in previous VLBA 86 GHz images (Rioja & Dodson 2011; Nakamura & Asada 2013), although one of the early GMVA images presented by Krichbaum et al. (2006) suggested a hint of limb-brightening.

For a better description of the near-core structure, in the lower panel of Figure 4 we display the same image as in the upper panel but restored with a circular Gaussian beam whose diameter is equal to the minor axis of the synthesized beam in
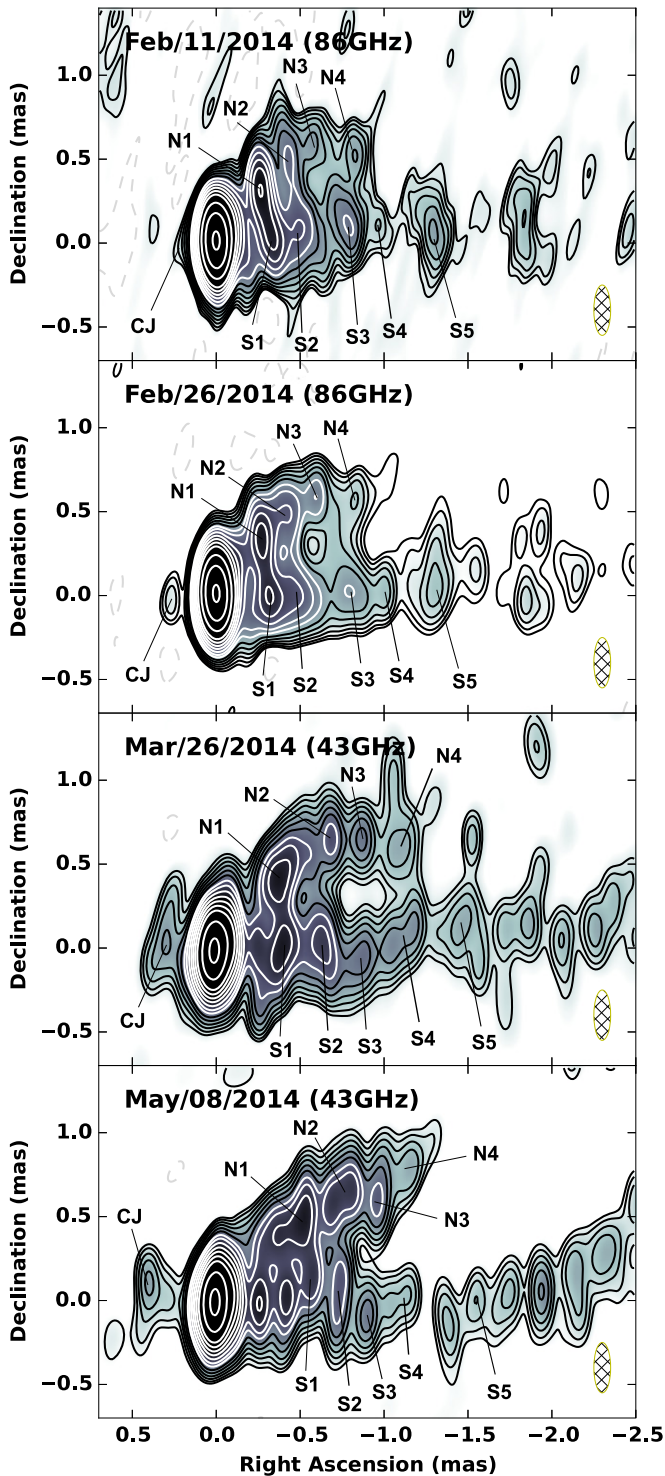
**Figure 6.** Multi-epoch images of the M87 jet. From the top, we show images observed on 2014 February 11 at 86 GHz, 2014 February 26 at 86 GHz, 2014 March 26 at 43 GHz, and 2014 May 8 at 43 GHz. All the images are convolved with a common beam of 0.30 mas × 0.11 mas at PA 0° (shown at the bottm-right corner of each panel). Contours on each image are −1, 1, $2^{1/2}$, 2, $2^{3/2}$, 4... times 1.0 mJy beam$^{-1}$ (upper two panels) and 2.0 mJy beam$^{-1}$ (lower two panels). The components with labels are the ones identified over the different epochs/frequencies consistently.
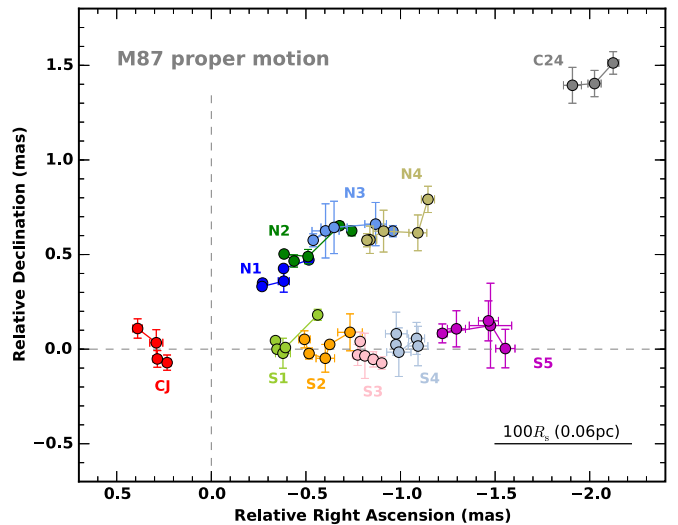


**Figure 7.** Observed sky positions of each component relative to the core. The components in the main jet are all moving in the western direction, while the counter jet component CJ is moving in the opposite direction (i.e., to the northeast).

$<28\ R_s$, projected) from the core with a large opening angle. We investigate the transverse jet structure in more detail in Section 3.3.

On the eastern side of the core, we detected weak but significant emission (at a level of 6σ in the combined image) at ~0.25 mas from the core (see the upper panel of Figure 4). This emission was also detected in the second-epoch-only image, but was marginally seen in the first-epoch-only image due partly to the lower sensitivity. The previous high-dynamic-range imaging of this jet at 15 and 43 GHz detected the counter emission in more detail (Kovalev et al. 2007; Ly et al. 2007; Acciari et al. 2009), and those authors conclude that the counter emission is a real counter jet. As described below, based on the observed proper motion and consistent detection at 43 GHz, we also conclude that the counter feature detected in the present observations is a real counter jet component emanated from the core.

In Figure 5 we also show a tapered image restored with a beam of 0.4 mas diameter to emphasize the larger-scale emission. Consistent with known lower-frequency images, the 86 GHz jet extends in the northwest direction on the large scale. In this period the southern limb is brighter within ~3 mas from the core, then the northern side rebrightens beyond that distance. Eventually the PA of the central jet axis results in ~293°, matching that in lower-frequency images.

### 3.2. Comparison with Lower-frequency Images

Although our 86 and 43/24 GHz observations were not simultaneous but 10 days to 10 weeks apart, it is still useful to compare them to examine any structural consistency or variations. In fact, their comparable image dynamic ranges at a level greater than 1000 to 1 allow a reliable image comparison between 86 GHz and the lower frequencies for the first time.

#### 3.2.1. Jet Morphology

In Figure 6 we show a sequence of our 86 and 43 GHz images, where all the images are restored with the same

the upper panel. The jet-launching morphology within ~0.5 mas from the core appears to be complicated, but one obvious feature found in this image is that the limb-brightened structure is already well developed at <0.2 mas (equivalent to

**Table 3**
Motion of Components

| Feature | $r$ | PA | $\mu$ | $\beta_{\mathrm{app}}$ |
|---|---|---|---|---|
| | (mas) | (deg) | (mas yr$^{-1}$) | ($v_{\mathrm{app}}/c$) |
| (a) | (b) | (c) | (d) | (e) |
| CJ | $0.25 \pm 0.05$ | $106 \pm 8$ | $-0.63 \pm 0.29$ | $-0.17 \pm 0.07$ |
| N1 | $0.44 \pm 0.01$ | $322 \pm 1$ | $1.22 \pm 0.08$ | $0.32 \pm 0.02$ |
| N2 | $0.64 \pm 0.04$ | $317 \pm 2$ | $1.65 \pm 0.15$ | $0.44 \pm 0.04$ |
| N3 | $0.86 \pm 0.16$ | $316 \pm 2$ | $1.45 \pm 0.16$ | $0.38 \pm 0.04$ |
| N4 | $1.01 \pm 0.08$ | $304 \pm 4$ | $1.81 \pm 0.46$ | $0.48 \pm 0.12$ |
| S1 | $0.34 \pm 0.02$ | $277 \pm 1$ | $1.00 \pm 0.02$ | $0.26 \pm 0.03$ |
| S2 | $0.49 \pm 0.05$ | $275 \pm 2$ | $1.64 \pm 0.01$ | $0.43 \pm 0.03$ |
| S3 | $0.78 \pm 0.05$ | $272 \pm 2$ | $0.31 \pm 0.18$ | $0.08 \pm 0.05$ |
| S4 | $0.98 \pm 0.13$ | $274 \pm 2$ | $0.58 \pm 0.50$ | $0.15 \pm 0.13$ |
| S5 | $1.29 \pm 0.11$ | $274 \pm 3$ | $1.25 \pm 0.61$ | $0.33 \pm 0.16$ |
| C24 | $2.36 \pm 0.11$ | $306 \pm 3$ | $1.34 \pm 0.65$ | $0.35 \pm 0.17$ |

**Note.** (a) Component name. (b), (c) Radial angular distance and position angle of the component from the core on 2014 February 11 (on March 8 for C24). (d) Best-fit proper motion value. (e) Corresponding apparent speed in units of the speed of light.

convolving beam of 0.30 mas × 0.11 mas at PA 0°, which is approximately an intermediate resolution between 86 and 43 GHz. The overall jet shape and characteristic structure are in good agreement with each other. It is known that the M87 jet is relatively smooth and less knotty, but here we do see some noticeable features or patterns in the jet when imaged at the high resolution. As shown in Figure 6 we identified several components in both 86 and 43 GHz images consistently, including a counter jet component (which is more prominent at 43 GHz). These features are marked as CJ (counter jet), N1–N4 (in the northern limb), and S1–S5 (in the southern limb). Since these components are typically $\gtrsim 0.2$ mas/$\gtrsim 0.4$ mas apart from each other in east–west/north–south directions, we could identify them separately regardless of the shape of applied convolving beam between 86 and 43 GHz. At 24 GHz, the larger beam size led to the mix of adjacent components, precluding us from identifying these inner components separately. In our 24 GHz images we instead identified another component at ~2 mas downstream of the jet (in the northern limb), which is marked as C24.

### 3.2.2. Proper Motions

While these components were consistently identified over the observed period, they were indeed gradually moving in the jet. In Figure 7 we show the observed positions of these components with respect to the core over the monitoring period. For each component the position was measured by fitting an elliptical Gaussian model with the AIPS task JMFIT, and its position uncertainty was estimated as the fitted size divided by the peak-to-noise ratio (Fomalont 1999). The measured proper motion results are summarized in Table 3. Note that there may be an absolute position offset between the 86 and 43 GHz cores due to core-shift. However, such a shift is expected to be only ~20 $\mu$as (assuming the $\nu^{-0.94}$ dependence determined at low frequencies; Hada et al. 2011), which is quite small compared to the proper motions observed in the present study.

In the main jet the mean speed of the observed components is $\beta_{\mathrm{app}} = 0.32$, where most of them are moving at a similar speed in the range of 0.3–0.5c. On the other hand, the counter

jet CJ is moving in the opposite direction (to the northeast) at a slightly slower speed of ~0.17 c. These values observed in both the jet and counter jet are similar to those suggested by Ly et al. (2007), although at that time the measurement was based on only one pair of VLBA 43 GHz observations separated by more than six months. Note that S3 and S4 appear to be quite slow or quasi-stationary compared to the rest of the features in the main jet. For these features we cannot completely rule out the possibility of component misidentification among the different epochs. However, looking at the overall evolution of the jet morphology within ~1 mas from the core, the northern limb gets more elongated than the southern limb during our monitoring period (see Figure 6). It therefore seems that an asymmetry exists in jet apparent motions between the northern and the southern limbs, which is consistent with the measured slow motions of S3 and S4. The presence of quasi-stationary components in the subpc jet of M87 is also suggested by Kovalev et al. (2007) based on long-term VLBA 15 GHz monitoring. We did not see clear signatures of the faster ($\gtrsim 1c$) motions as reported in Walker et al. (2008) and Acciari et al. (2009).

### 3.2.3. Spectra

Comparing the closest pair of data on February 26 (at 86 GHz) and March 8 (at 43 GHz), the observed peak brightness in each image (when measured with a common 0.3 mas × 0.1 mas beam as in Figure 6) is 530 mJy beam$^{-1}$ (at 86 GHz on February 26) and 546 mJy beam$^{-1}$ (at 43 GHz on March 8). This results in a non-simultaneous (but still close-in-time) 43/86 GHz spectral index of the core (at this resolution) being flat ($\alpha_{c,43/86} \sim -0.04$), indicating that the M87 core is substantially self-absorbed up to 86 GHz.

Considering the significant proper motions as well as the variable nature of the individual components in the extended jet, it is difficult to obtain an accurate map of the spectral index distribution with the present non-simultaneous 43/86 GHz images. Hence, here we examined only spatially integrated spectra for the main and counter jets in the following way. For the main jet, we compared the integrated flux densities (sum of CLEAN components) between the two frequencies for an area from 0.2 mas to 1.2 mas along the jet, corresponding to the inclusion of N1–N4 and S1–S4. We obtained an integrated spectral index of $\alpha_{j,43/86} = -0.8 \pm 0.3$ for this region. For the same region, we also checked a spectral index between 24 and 43 GHz using our data, and obtained a value of $\alpha_{j,24/43} = -0.6 \pm 0.3$. These two values are consistent within the errors, although a possible spectral steepening might exist at >43 GHz due to the higher cooling efficiency.

As for the counter jet, the observed spectrum between 43 and 86 GHz seems to be steeper than that of the main jet ($\alpha_{cj, 43/86} \sim -1.8$). However, the uncertainty is still large due to its weak nature.

### 3.2.4. Brightness Ratio of Jet to Counter Jet

Given that the brightness profile of the main jet is very rich while the counter jet is weak and less characterized, there is a large uncertainty in determining the exact value of brightness ratio (BR) of jet to counter jet.

Here we consider the following possibilities to estimate BR: (1) CJ is the counterpart of S1; (2) CJ is the counterpart of S2. The choice of (1) is because CJ and S1 are symmetrically
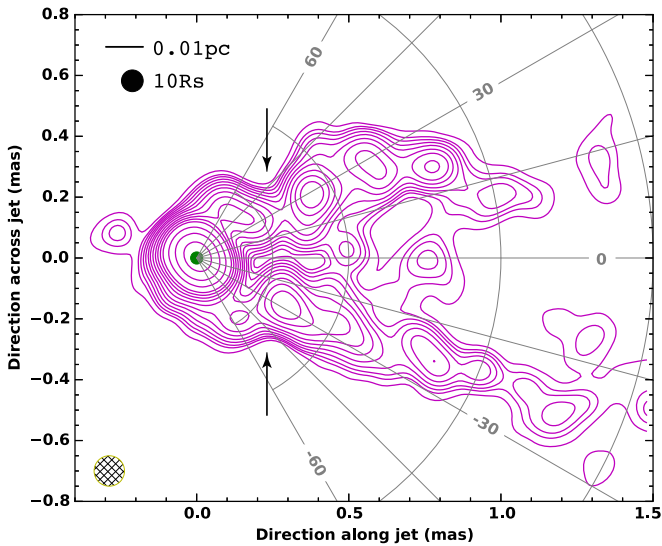
**Figure 8.** Close-up view of the innermost region of the M87 jet observed with VLBA+GBT at 86 GHz. The image is restored with a 0.11 mas circular Gaussian beam, which is equivalent to that of the minor axis of the synthesized beam. The image is rotated on the sky by $-23°$ in order to align the jet central axis to the horizontal direction. For reference, on the origin of the coordinates we place a green-colored circle with a diameter of 40 $\mu$as, which is equivalent to the size of the 230 GHz core reported by Doeleman et al. (2012). The arrows indicate where the jet shape is locally shrinking.

located with respect to the core, while case (2) is also possible if we additionally consider the relativistic "arm-length ratio" that reflects apparent motions differing by a factor of $\sim$2 between the jet and the counter jet.

In the case of (1), when compared using the total flux densities, the BR is 25.2 at 86 GHz or 5.7 at 43 GHz. In the case of (2), the BR is 22.0 at 86 GHz or 4.4 at 43 GHz. Alternatively, if we use the peak flux densities, the BR is 25.3/4.7 at 86/43 GHz for case (1), or 21.4/5.6 at 86/43 GHz for case (2).

It is not clear yet whether the resulting difference in BR between 86 and 43 GHz is real or not. We consider that the measurements at 43 GHz would be more secure due to the higher S/N for the counter jet. Conservatively, here we conclude that the BR is between $\sim$5 and $\sim$25 within the central 1 mas region.

### 3.3. Transverse Jet Structure

Resolving a jet in the direction transverse to its axis is important for understanding the opening angle, collimation efficiency, and possible velocity gradient across the jet. To perform this, one needs a high-quality image at a sufficient angular resolution across the jet. The new 86 GHz image presented here allows us to analyze the detailed transverse structure of the jet-launch region near the black hole.

In Figure 8 we show a close-up view of the innermost region of the M87 jet. For a better description across the jet, the image is restored with a circular Gaussian beam whose FWHM is equivalent to that of the minor axis of the synthesized beam. This is the same contour image as that in the lower panel of Figure 4, but here the image is rotated on the sky by $-23°$ in order to align the jet central axis with the horizontal axis.

A strongly limb-brightened profile is evident beyond 0.5 mas from the core, as consistently seen in the 43 GHz images. Within 0.5 mas of the core, the limb-brightening is continuously visible. It is notable that the limb-brightened jet is already formed at a distance of 0.15 mas from the core. Moreover, one
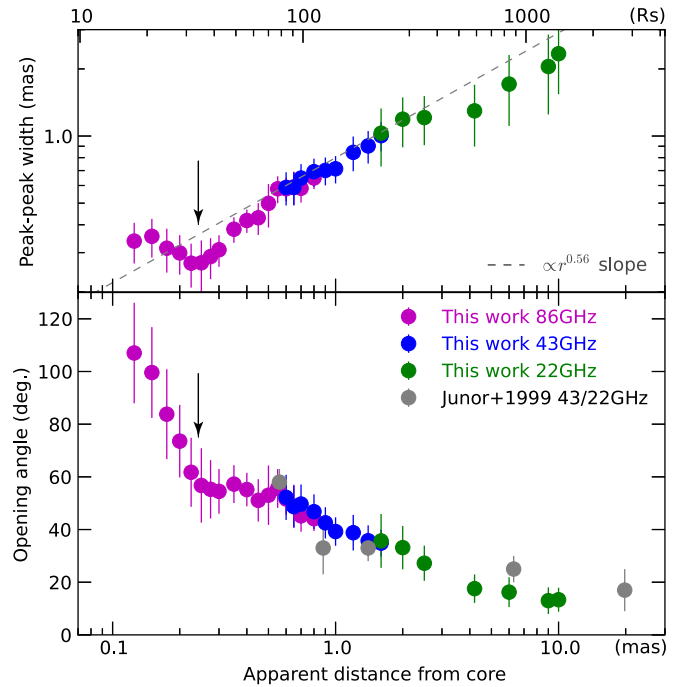


**Figure 9.** Radial profiles of the transverse structure of the M87 jet. The upper panel indicates a jet width profile $W_{pp}(r)$, which is obtained by measuring the peak-to-peak separation of the two limbs at each $r$ from the core. The gray dashed line represents a dependence $\propto r^{0.56}$, which was determined in our previous extensive measurement of jet width between $r \sim 1$ mas and $r \sim 400$ mas from the core (Hada et al. 2013). The dashed line plotted here is not fitted to the data but is arbitrarily placed just for reference. The lower panel shows the corresponding apparent opening angle profile $\phi_{pp}(r) \equiv 2\arctan(W_{pp}(r)/2r)$. The data points with gray color are previous results by Junor et al. (1999) and Biretta et al. (2002). In both panels the data colored magenta, blue, and green refer to 86, 43, and 24 GHz, respectively. The arrow in each panel corresponds to the location of the arrow in Figure 8.

more remarkable feature near the core is that the limb-brightened jet is evolving in a highly complicated manner; in particular, there is a "constricted" structure at $\sim$0.2–0.3 mas from the core, where the jet appears to be shrinking locally. One might be concerned that this structure can be artificially produced due to insufficient deconvolution accuracy, since the original synthesized beam of our 86 GHz array is elongated in the northeast–southwest direction, which could particularly affect the near-core shape of the northern limb. However, we conclude that this is not an artifact. The root of the northern limb at 0.1–0.2 mas from the core is relatively knotty, and we were required to put relatively strong CLEAN components in our deconvolution process. Thus this feature was distinguishable from the central core emission. As an independent test, we also examined the fidelity of our super-resolution image at 86 GHz using the sparse modeling technique (Honma et al. 2014), and obtained a consistent structure within 0.2 mas of the core. Details about the application of this technique to the present data will be described in a forthcoming paper. We additionally note that the corresponding structure is marginally seen also in our 43 GHz images (as a "neck" of intensity between the core and N1/S1; see, e.g., the middle panel of Figure 6), suggesting that this structure is sustained at least during our monitoring period (a few months).

Using Figure 8, we analyzed the radial evolution of the transverse jet structure in detail. The results are presented in Figure 9, where we supplemented lower-frequency
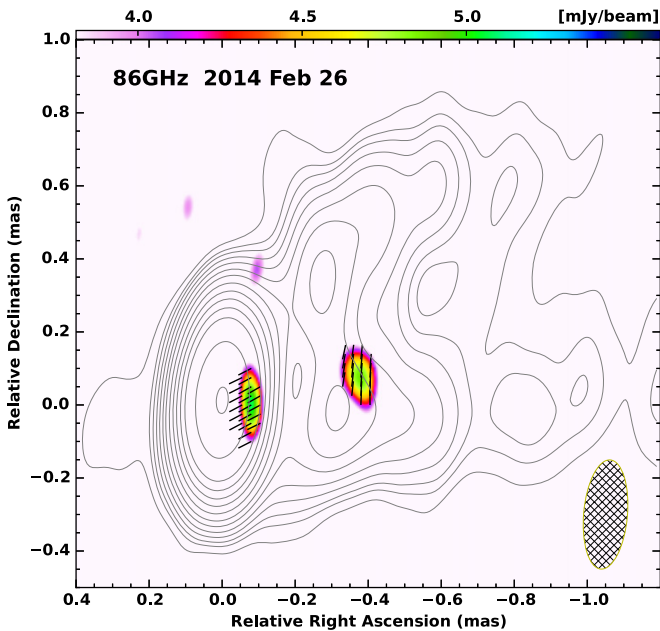
**Figure 10.** VLBA+GBT 86 GHz polarimetric result for M87 on 2014 February 26. The color map, the vectors, and the contours indicate the observed polarized intensity, the observed EVPA, and the total intensity distribution, respectively. The convolving beam is shown at the bottom-right corner. The polarized intensity (color map) is displayed from the $4\sigma$ rms noise level. The contours show 1, 2, $2^{3/2}$, 4... times 2.1 mJy beam$^{-1}$.

measurements at 43 and 24 GHz further down the jet. The upper panel indicates the observed jet width profile $W(r)$, while the lower panel plots the corresponding (apparent) opening angle profile $\phi(r) \equiv 2\arctan(W(r)/2r)$, assuming that the jet origin is infinitesimally small. We defined $W(r)$ here as the peak-to-peak separation of the two limbs perpendicular to the jet axis (thus, for clarity, we redenote the present measurements as $W_{pp}(r)$ and $\phi_{pp}(r) \equiv 2\arctan(W_{pp}(r)/2r)$) rather than the usual separation from outer edge to outer edge that would be more appropriate for expressing an "entire jet width." The reason why we use $W_{pp}$ here is because measurements of peak-to-peak separation are less affected by the applied convolving beam, while measurements based on the outer edges are more sensitive to the beam size. This is particularly relevant to the near-core region where the jet cross section is comparable to or even smaller than that of the synthesized beam. Our present purpose is not to determine an absolute width of the jet but rather to measure a radial dependence of the jet evolution as close to the core as possible by using a specific streamline in the jet. In this respect, $W_{pp}$ is a proper way that allows us to use a super-resolution image and thus to quantify the streamline closer to the core. We note that the radial dependence of $W_{pp}(r)$ can be different from that of $W(r)$. This should in fact be an interesting topic to examine, but determining the difference between them in detail is beyond the scope of our present work. Such an advanced analysis of the jet profile is indeed possible by taking advantage of the sparse modeling technique mentioned above, and hence will be presented in a forthcoming paper.

The following interesting features are found in Figure 9. Beyond 0.5–0.6 mas from the core, the measured jet shape is well described by a parabolic collimation profile. There are several previous measurements of jet width and opening angle on this scale. For the jet width, Asada & Nakamura (2012) and

Hada et al. (2013) determined the radial profile to be $W(r) \propto r^{0.56\pm0.03}$ at distances from $\sim$1 mas to $\sim$500 mas from the core, and the present $W_{pp}(r)$ beyond 0.5 mas is in good agreement with this dependence. The opening angle was previously measured by Junor et al. (1999) and Biretta et al. (2002), and their finding of $\phi \sim 60°$ opening angle at 0.5 mas from the core is consistently seen in our result at the same distance.[10] On the other hand, closer to the core where our 86 GHz image can access, the jet profile becomes more complicated. From the distance of 0.6 mas to 0.3–0.2 mas where the constriction exists, the observed opening angle remains roughly constant at $\phi_{pp}(r) \sim 60°$, indicating the jet to have a conical geometry. Then, even closer to the core, within $\sim$0.25 mas, the jet widens again by a factor of 1.5–2. As a result, the apparent opening angle increases rapidly from $\sim$60° up to $\gtrsim$100° in this region. This trend can be recognized in Figure 8 with the guide of polar coordinates. If the opening angle is defined with respect to $W(r)$ instead of $W_{pp}(r)$, the value should be even larger.

Note that the opening angle may become smaller if the jet-launch point has a finite size (cross section). However, all previous EHT observations of M87 at 230 GHz constrained the jet-launch size to be remarkably small (40 $\mu$as; Doeleman et al. 2012; Akiyama et al. 2015). For reference, we superpose the corresponding model of the 230 GHz core on the coordinate origin of Figure 8. As seen from this map, the modification of the opening angle is sufficiently small at our scale of interest, so our assumption should be reasonably valid. Therefore, this is the largest opening angle ever observed in any astrophysical jet including M87 itself.

### 3.4. Polarimetry

In Figure 10 we show a result of our 86 GHz polarimetry analysis for the M87 jet. Here we display the data on February 26, since at this epoch the data quality is better and also we can perform the more reliable EVPA correction with the help of an external close-in-time VLBA observation of the calibrator 3C 273 (see the Appendix for more details). The result on February 11 is essentially consistent with Figure 10, although the S/N is lower than that on February 26.

Given that the M87 jet is only weakly polarized (or highly depolarized) on pc-to-subpc scales, presumably due to a dense foreground Faraday screen (Zavala & Taylor 2002), it is still challenging to discover the whole polarimetric structure of this jet from the present observation. Nevertheless, we indeed detected some significant polarized emission in a few parts of the jet at S/N $\sim$ 4.5. One polarized feature was detected at 0.1 mas downstream of the core. This feature has a polarized intensity of 5.0 mJy beam$^{-1}$, and its fractional polarization is at a level of 3%–4%. On the other hand, we detected another polarized feature at 0.4 mas downstream in the jet. While this feature has a similar polarized intensity (4.9 mJy beam$^{-1}$), the observed fractional polarization becomes as high as 20%. Since the previous VLBI polarimetric observations of this jet (which are usually made at 15 GHz or lower frequencies) reported a fractional polarization up to 11.5% (Junor et al. 2001), this is the highest fractional polarization ever reported on pc-to-subpc scales of this jet. This polarized feature appears to be located at

---

[10] In Junor et al. (1999) and Biretta et al. (2002) the opening angle is defined with respect to the full width at quarter-maximum (FWQM) on slice profiles of jet intensity. This gives a slightly larger opening angle than that in our method at the same $r$.

the boundary of S1 and the central "valley" of emission (the so-called "spine" part of the jet).

Regarding EVPA, the near-core feature shows a mean EVPA direction along the jet, while the near-S1 feature indicates a mean EVPA roughly perpendicular to it. If this is the case, the corresponding magnetic-field-vector polarization angle (MVPA) of the near-core/near-S1 features is perpendicular/parallel to the jet axis, respectively. However, we recall that there is still a large uncertainty in our EVPA correction procedure ($\Delta\chi_{M87} \sim \pm 20°$; see Section 2.2 or the Appendix). Moreover, there might be an additional external EVPA rotation if there is a significant amount of the foreground Faraday screen toward M87 (e.g., $\Delta\chi_{RM,M87} = RM \lambda_{3.5\,mm}^2 \sim 7°$ if $RM \sim 10^4$ rad m$^{-2}$). This does not permit us to fix the intrinsic EVPA definitively.

## 4. DISCUSSION

### 4.1. Jet Viewing Angle and Speed

The viewing angle $\theta$ of the M87 jet has been discussed for a long time and it remains a puzzling issue. Owen et al. (1989) suggest that the jet is not too far out of the plane of the sky ($\theta \gtrsim 45°$) based on the patterns of the helically wrapped filaments seen in the kpc-scale VLA jet. On pc-to-subpc scales Ly et al. (2007) suggest $\theta \sim 30°–45°$ based on a measurement of proper motion and brightness ratio with VLBA at 43 GHz. On the other hand, a strong constraint is obtained from optical observations of the active knot HST-1 at $\sim 0.''8$ from the nucleus, where Biretta et al. (1999) found superluminal motion up to $6c$, tightly requiring $\theta$ to be less than 19° from our line of sight. Perlman et al. (2011) also suggest a similar range ($\theta \sim 11°–19°$) based on the optical polarization properties of HST-1.

In the present study, we estimate $\theta$ near the jet base based on the measured apparent motions in the jet and the counter jet, such that $\frac{\mu_j}{\mu_{cj}} = \frac{1 + \beta_{int}\cos\theta}{1 - \beta_{int}\cos\theta}$, on the assumption that the bidirectional jet is intrinsically symmetric. If we compare CJ with S1 or S2 (as explained in Section 3.2.4), the proper motion ratio results in $\mu_j/\mu_{cj} = 1.5–2.5$. Searching for a common area with $\mu_j = \frac{\beta_{int}\sin\theta}{1 - \beta_{int}\cos\theta}$, we then obtain solutions of $\theta$ and $\beta_{int}$ to be $\theta = 29°–45°$ and $\beta_{int} = 0.29–0.50$. With these ranges of $\theta$ and $\beta_{int}$, we can also estimate an expected BR, and this results in a range of BR = 2.6–8.7 (assuming a continuous jet model with $\alpha = -0.7$), which is consistent with the observed BR in our 43 GHz images. Therefore, our estimate of $\theta$ is rather similar to those suggested in Ly et al. (2007), whose measurement was also made at a similar distance from the core. In contrast, the derived range of $\theta$ is larger than that obtained from the optical HST-1 kinematics.

We do not rule out the possibility of the smaller $\theta$ as suggested from the HST-1 observations, since there can still be an overlap ($\theta > 14°$) if we allow the maximum proper motion ratio ($\mu_j/\mu_{cj} = 4.6$) within the $1\sigma$ errors. Also, a recent VLBA monitoring program of the inner jet at 43 GHz by Walker et al. (2008) suggests a fast apparent motion (in the main jet) of $\sim(1–2)c$, which might favor a small viewing angle. Thus more accurate measurements of proper motion as well as brightness ratio are important in future studies.

One issue we should note, however, is that the M87 jet is highly limb-brightened. A commonly invoked explanation for limb-brightening structure in relativistic jets is that there is a velocity gradient transverse to the jet, such that the flow speed becomes faster toward the jet's central axis (e.g., Ghisellini et al. 2005; Nagai et al. 2014). According to this idea, the brighter part of the jet (i.e., the limb/sheath) has a larger Doppler factor $\delta$ ($\delta \equiv [\Gamma(1 - \beta\cos\theta)]^{-1}$ where $\Gamma$ is the bulk Lorentz factor) to the observer, while the dim part of the jet (i.e., the central spine) has a smaller $\delta$ due to the lower beaming relative to the sheath. Since $\delta(\beta)$ reaches a maximum at $\beta = \cos\theta$, if we consider the case of $\theta = 10°–20°$, the faster $\beta$ yields the larger $\delta$ for most $\beta$ unless $\beta_{spine}$ is unrealistically higher than $\beta_{sheath}$. This results in $\delta_{spine} > \delta_{sheath}$, indicating that the jet brightness profile would lead to a *ridge-brightened* structure. On the other hand, if we consider the case of $\theta = 29°–45°$, $\delta$ reaches a maximum at $\beta \sim 0.70–0.87$. $\delta$ then starts to decrease beyond this $\beta$, which in principle can reproduce a limb-brightened intensity profile.

Therefore, the observed limb-brightened structure of M87 may not be simply explained by a transverse velocity gradient alone if $\theta = 10°–20°$, requiring some other process to be at work (e.g., Lobanov & Zensus 2001; Stawarz & Ostrowski 2002; Gopal-Krishna et al. 2007; Zakamska et al. 2008; Clausen-Brown et al. 2011).

An alternative hypothesis to accommodate the apparent discrepancy in $\theta$ between the inner jet and HST-1 is that the viewing angle of M87 is not constant all the way down the jet. Our long-term VLBI monitoring of HST-1 has recently revealed significant variations in the observed PAs (from PA $\sim 270°$ to PA $\sim 310°$) of the substructures' trajectories (Giroletti et al. 2012; Hada et al. 2015).[11] This implies a deprojected (intrinsic) change in direction to be $\sim 10°$ (for a fixed $\theta = 15°$). Thus, it would not be surprising if $\theta$ of HST-1 is also variable at this level, and the fastest $\sim 6c$ speed could be seen when its $\theta$ is maximally beamed to us. Such a local misalignment of $\theta$ from the central jet axis can be realized if the HST-1 complex is traveling along a three-dimensional helical trajectory with respect to the central jet axis.

From the point of view of the high-energy emission, the jet base of M87 is proposed to be a likely site of the very-high-energy (VHE) $\gamma$-ray production (e.g., Aharonian et al. 2006; Acciari et al. 2009; Abramowski et al. 2012; Hada et al. 2012, 2014). The detection of VHE $\gamma$-ray emission is usually favored by a small viewing angle of the jet, which may also be opposed to the viewing angle derived above. However, it is interesting to note that the jet base of M87 has a very wide apparent opening angle, up to $\phi_{app} \sim 100°$ (Figures 8 and 9). If we consider the case of $\theta = 30°$, the intrinsic opening angle is estimated to be $\phi_{int} \sim \phi_{app} \times \sin\theta = 50°$. This means that the near side of the sheath is almost pointing toward us at $\theta_{near} \sim 5°$ close to the jet base (assuming an axially symmetric jet). This value is quite similar to the typical viewing angle in blazars. Therefore, the observed VHE emission from the jet base could be associated with a locally beamed substructure in the near side of the sheath (e.g., Lenain et al. 2008; Giannios et al. 2010).

We also note that the bulk flow speed near the jet base may be somewhat faster than the component speeds we measure. In fact, $\beta_{int}$ derived from the proper motion ratio $\mu_j/\mu_{cj}$ is applicable to both bulk and pattern speeds, and one cannot distinguish between these two with such a measurement alone. A bulk flow speed is more directly related to the brightness ratio BR. The expected BR of 8.7 described above (with $\beta_{int} = 0.5$ and $\theta = 29°$) is actually

---

[11] Changes in position angle of parsec-scale superluminal components are also seen in another nearby radio galaxy, 3C 120 (Gómez et al. 2000, 2001; Casadio et al. 2015).

only partially consistent with the present observations (i.e., still inconsistent with the measured BR at 86 GHz), and this situation is essentially the same for a smaller angle of, e.g., $\theta = 15°$ (BR = 11). To reproduce the observed BR in our 43/86 GHz images fully consistently, we suggest that the bulk flow speed needs to be faster than $\sim 0.6\,c$ at this location.

### 4.2. Confinement of Magnetized Jet by Hot Accretion Flow/Corona?

One of the most intriguing features found from our 86 GHz observation is that the initial jet formation structure evolves in a quite complicated manner; there are multiple stages before the jet finally reaches the well-defined parabola in the outer scale. The jet is formed with $\phi_{app} \sim 100°$, then rapidly collimated into $\phi_{app} \sim 60°$ within $\sim 0.25$ mas (a projected distance of $\sim 35\,R_s$) from the core, and subsequently reaches the "constricted" point. From there, the jet expands roughly conically at $\phi_{app} \sim 60°$ until $\sim 0.6$ mas ($\sim 84\,R_s$, projected) down the jet, and finally enters the large-scale parabola collimation zone. A possible structural change of the jet profile near the black hole was originally suggested in Hada et al. (2013). While this kind of feature might be self-formed through some instabilities (such as the sausage-pinch instability in a magnetohydrodynamic flow; e.g., Begelman 1998), it may also be a signature of the interaction of the jet with the surrounding medium. In fact, there are growing implications that pressure support from an external medium is necessary to create an efficient collimation of a jet (e.g., Nakamura et al. 2006; Komissarov et al. 2007, 2009). Therefore, in what follows we discuss whether the formation of the M87 jet on this scale can be subject to an external effect or not, based on a simple comparison of the pressure balance between the jet ($p_{jet}$) and the external medium ($p_{ext}$).

Here we consider the case that the internal pressure of the M87 jet is approximated by the sum of the leptons ($p_\pm$) and the magnetic fields ($p_B$), and that the relative contribution from protons is small (Reynolds et al. 1996). In Kino et al. (2014), we examined the allowed range of the energy balance between electrons and magnetic fields at the base of this jet based on the synchrotron self-absorption (SSA) theory, and showed that the radio core at 43 GHz can be highly magnetized or at most roughly in equipartition ($10^{-4} \lesssim U_e/U_B \lesssim 0.5$)[12] unless the power index of the electron energy distribution is too steep (i.e., unless $q > 3$ where $n_e(E_e) \propto E_e^{-q}$). The observed spectral index for the optically thin part of the jet in our 24/43/86 GHz images ($\alpha_j \sim -0.6$ to $-0.8$, i.e., $q \sim 2.2$–$2.6$ where $q \equiv -2\alpha + 1$ in the present definition) satisfies this condition. In this case, the total pressure of the jet is predominantly due to the magnetic fields, or the particle pressure is at most of the same order of magnitude as the magnetic one. Therefore, we can reasonably adopt that $p_{jet} \sim p_B = B^2/8\pi$ at the 43 GHz core. As for the 86 GHz core, we can similarly estimate its $B$ value based on the SSA formula (Equation (11) in Kino et al. 2014) in combination with the modelfit parameters listed in Table 2, and this results in $B_{core,86} \sim 8.3$ G. This value is just in between $B_{core,43}$ and $B_{core,230}$ derived in Kino et al. (2014, 2015), and a magnetically dominated state can be consistently satisfied. Thus adopting this $B_{core,86}$, we obtain

$p_{B,core,86} \sim 2.7$ dyn cm$^{-2}$. For the jet downstream of the core, $p_B$ depends on the radial profile of the magnetic fields. In any case, to support/confine the jet on these scales, the external medium needs to have a pressure that can be balanced by the suggested level of $p_{jet}$.

According to the observed $\nu^{-0.94}$ frequency dependence of the core-shift (Hada et al. 2011), the radio core at 86 GHz is estimated to be located at $\sim 3\,R_s$ from the black hole on the plane of the sky. This indicates the deprojected distance of the 86 GHz core to be between $\sim 6\,R_s$ and $\sim 12\,R_s$ for a range of $\theta = 15°$ or $\theta = 30°$, respectively. On these scales a likely source of the external confinement medium may be the inner part of the accretion flow or associated coronal region (McKinney 2006; McKinney & Narayan 2007). Since the accretion rate onto the M87 nucleus is significantly sub-Eddington (Di Matteo et al. 2003), the accretion mode of the M87 black hole is thought to be an advection-dominated, hot accretion flow state (ADAF; e.g., Narayan & Yi 1994). As an ADAF is geometrically thick and roughly approximated by a spherically symmetric structure, such a configuration may be suitable in shaping/confining the initial stage of a jet. While the original ADAF assumed a radially constant mass accretion rate ($\dot{M}$), subsequent theoretical studies favorably suggest that $\dot{M}$ decreases with decreasing radius due to convection (Quataert & Gruzinov 2000) or outflows (Blandford & Begelman 1999). In fact, the recent polarimetric study for the M87 nucleus at 230 GHz has derived $\dot{M}$ at $r \sim 21\,R_s$ from the black hole to be $\dot{M} < 9.2 \times 10^{-4}M_\odot$ yr$^{-1}$ (Kuo et al. 2014), which is more than 100 times smaller than that measured at the Bondi radius ($\dot{M}_{Bondi} \sim 0.1\,M_\odot$ yr$^{-1}$ at $r_{Bondi} \sim 230$ pc $\sim 4 \times 10^5\,R_s$; Di Matteo et al. 2003). For such modified ADAF flows, Yuan et al. (2012) and Yuan & Narayan (2014) present an updated set of self-similar solutions by taking into account radially variable $\dot{M}$ (i.e., $\dot{M}(r) \propto r^s$ where $s \sim 0.5$–1). Among these solutions, the pressure profile is described as $p_{ADAF}(r) \approx 1.7 \times 10^{16}\alpha_{visc}^{-1}m_{BH}^{-1}\dot{m}_{BH}r^{-5/2+s}$ dyn cm$^{-2}$, where $\alpha_{visc}$, $m_{BH}$, and $\dot{m}_{BH}$ are the dimensionless viscosity parameter, $M_{BH}/M_\odot$, and $\dot{M}_{BH}/\dot{M}_{Edd}$ ($\dot{M}_{Edd} \equiv L_{Edd}/0.1c^2$), respectively.[13] For $\dot{M}_{BH}$ onto the black hole, here we assume $\dot{M}_{BH}(r = R_s) \sim 10^{-4}M_\odot$ yr$^{-1}$ together with $s = 0.6$. These values are selected so that the extrapolated values of $\dot{M}(r)$ at $r = r_{Bondi}$ and $r = 21\,R_s$ consistently satisfy the above observations, and thus would be a reasonable combination of $\dot{M}_{BH}$ and $s$. With these values, we finally obtain $p_{ADAF}(r) \sim 2.2\alpha_{visc}^{-1}r^{-1.9}$ dyn cm$^{-2}$. Therefore, if we assume $\alpha_{visc}$ to be of the order of $10^{-2}$ (e.g., Yuan et al. 2012), the ADAF pressure results in $p_{ADAF} \sim 2.7$ dyn cm$^{-2}$ at $r = 10\,R_s$. Interestingly, this is quite comparable to $p_{jet}$ estimated at the 86 GHz core. Hence, we suggest that the pressure support from the inner part of the hot accretion flow may be dynamically important in shaping and confining the launch stage of the M87 jet.

Given that the external pressure contribution is significant at the jet base, the observed constricted structure at a projected

---

[12] The equipartition range cited here (which is originally from Kino et al. 2014) was derived, for simplicity, on the assumption that the underlying magnetic-field configuration is isotropic (Equation (11) in Kino et al. 2014). However, the same formula is also applicable for the case of an ordered magnetic-field geometry just by multiplying the total field strength by a small modification factor of $1/\sqrt{3}$ (see the more detailed explanation in that paper).

[13] The self-similar solutions presented in Yuan et al. (2012), Yuan & Narayan (2014), and also Narayan & Yi (1994) (for the original ADAF) are obtained using a height-integrated system of equations. Thus "$r$" in this case corresponds to the cylindrical radius, not the spherical radius from the central black hole. However, the effect of the vertical integration is examined in detail by Narayan & Yi (1995), and they proved that the height-integrated solutions are quite accurate approximations (within $\sim 10\%$ for the pressure) of the exact (spherically averaged) solutions in the limit of an advection-dominated state. Hence, we can reasonably consider that $r$ in the height-integrated solutions corresponds to the radial distance from the black hole.

distance of $\sim$35 $R_s$ from the core may reflect some important physical signature resulting from the jet-surrounding interaction. One possibility is that this feature marks a reconfinement node of the flow (e.g., Gómez et al. 1997; Komissarov & Falle 1997; Daly & Marscher 1988; Kohler et al. 2012; Matsumoto et al. 2012; Mizuno et al. 2015). Such a flow reconfinement can be realized if the radial profile of the external pressure downstream of the core decreases more slowly than that of the jet pressure. Alternatively, this constriction might be a signature of the sudden "breakout" from the central dense confining medium (presumably ADAF/hot corona), analogous to a jet in gamma-ray bursts (e.g., Morsony et al. 2007). If the breakout is the case, one may constrain the scale height (thickness) of the central confining medium to be of the order of $H \sim 2 \times 35 \times (\sin\theta)^{-1} = 140\,R_s$ (for $\theta = 30°$).

We note that the above discussion still leaves a considerable uncertainty in each parameter space and the actual force balance at the jet boundary may be more complicated (e.g., if the jet ram pressure at the boundary is significant or if there exists some instability in the accretion flow). In particular, the deep 86 GHz images obtained here provoke the following simple question: why is the suggested hot accretion flow still not detected in emission, despite the fact that an accretion scale well below $100\,R_s$ near the black hole is already imaged? This issue should be explored by future higher-sensitivity imaging observations (e.g., including the phased-up ALMA; Fish et al. 2013). Also, the lack of additional 86 GHz images at different epochs with a similar sensitivity does not permit us to conclude whether the observed constricted feature is a persistent structure or just a temporary one (although we note that the subsequent 43 GHz images in Figure 6 still show a hint of the corresponding feature at the same location). In any case, our simple order-of-magnitude estimate discussed here implies a non-negligible contribution of the external medium to the initial evolution of the M87 jet. Further VLBI monitoring of the jet base at 86 GHz will enable us to address this issue more definitively.

### 4.3. Implications for Faraday Screen and Magnetic Field Near the Jet Base

Finally we briefly discuss the polarization structure of the M87 jet. While polarimetric properties of this jet have been intensively studied on kpc scales in the radio and optical wavelengths (e.g., Owen et al. 1989; Perlman et al. 1999, 2011; Chen et al. 2011), the polarization structure is still highly uncertain on parsec-to-subparsec scales. This is because polarization signals from the M87 inner jet are generally quite low, presumably due to a dense foreground medium on these scales, as suggested by Zavala & Taylor (2002). They found an extreme RM distribution that varies from $-4 \times 10^3$ rad m$^{-2}$ to $>9 \times 10^3$ rad m$^{-2}$ in the jet at 20 mas (1.6 pc, projected) from the core. Recently, Kuo et al. (2014) performed the first RM measurement toward the nucleus in the 230 GHz band with the Submillimeter Array. Although the angular resolution in their study is limited to $\sim 1''$, they suggested the value of RM near the central black hole to be within $(-7.5$ to $3.4) \times 10^5$ rad m$^{-2}$, by assuming that the bulk of the 230 GHz emission originates in the jet base within $\sim 21\,R_s$ from the black hole.

The detection of polarized signals in our 86 GHz VLBI images provides some important insights into the close vicinity of the central black hole of M87. First, the detection of a polarized feature at $\sim$0.1 mas ($\sim$14 $R_s$, projected) from the black hole provide evidence that the RM associated with this feature is not larger than a certain value. If we assume that the depolarization has an external origin and that the observed fractional polarization degree is given by $m(\lambda) = m_0 \exp(-2\sigma_{RM}^2\lambda^4)$ (where $m$, $m_0$, and $\sigma_{RM}$ are observed fractional polarization, intrinsic polarization, and standard deviation of the RM fluctuations, respectively; Burn 1966), the maximum $|\sigma_{RM}|$ is constrained to be $\sim(5.8$–$17) \times 10^4$ rad m$^{-2}$ (adopting $\sim e^{-1}$–$e^{-3}$ damping of $m_0$). This is consistent with $|\text{RM}| < 7.5 \times 10^5$ rad m$^{-2}$ obtained at a similar scale by Kuo et al. (2014). More dedicated VLBI polarimetric studies in future would be fruitful in revealing more detail of the spatial distribution of the RM near the jet base.

The second point is that we detected a fractional polarization of $\sim$20% in the region at $\sim$0.4 mas from the core, which is the highest value ever seen in the pc-to-subpc scales of this jet. Since the observed polarized signals are a consequence of multiple depolarization effects during propagation (internal/external Faraday depolarization, bandwidth/beam depolarization), the intrinsic fractional polarization must be higher than the observed one (e.g., in the manner mentioned above). Therefore, the observed highly polarized signal indicates the presence of a well-ordered magnetic field in this region. The origin of such an ordered field is still not clear, but a possible hint from our observation is that this feature is located at the boundary of the southern limb ("sheath") and the central valley of emission ("spine"), where the presumed velocity shear may amplify the longitudinal field component (e.g., Laing 1980). Interestingly, the observed EVPA for this feature (which is perpendicular to the jet) seems to be consistent with the shear interpretation, although the accuracy of the present EVPA calibration is still not fully adequate to confirm this scenario. Alternatively, the ordered field could be associated with a global helical/twisted field geometry, as predicted by the magnetically driven jet scenario (e.g., Broderick & Loeb 2009).

Ultimately, a further increase in the array sensitivity to total/polarized intensity is necessary, as well as the implementation of a better polarimetric calibration strategy. The upcoming incorporation of the Large Millimeter Telescope (Hughes et al. 2010) and of the phased-up ALMA to the millimeter VLBI network will be enormously powerful in this respect (Fish et al. 2013). This will allow us to image the magnetic field structure in the jet-launching site as well as the surrounding accretion flow structure in much more detail.

### 5. SUMMARY

We reported results obtained from a new high-sensitivity, high-resolution VLBA+GBT observation of the M87 jet at 86 GHz. We summarize our main results as follows.

1. We obtained a high-quality image of the jet-launch region of the M87 jet down to $\sim$10 $R_s$ near the black hole. The resulting image dynamic range is greater than 1500 to 1, which is the highest ever obtained for this source at 86 GHz. The high-sensitivity image clearly confirmed some important well-known features of this jet such as a jet launch with a wide opening angle, a limb-brightened intensity profile, a parabola-shape collimation profile, and a counter jet. The limb-brightened structure is already

well developed at $<28\,R_s$ (projected) from the core, and the corresponding apparent full-opening angle near the black hole becomes as broad as $\sim100°$. This is the broadest opening angle ever seen in any astrophysical jet including the M87 jet itself.

2. We discovered a complicated jet-launch shape near the black hole ($r \lesssim 100\,R_s$) in our 86 GHz image, indicating multiple collimation stages before the jet finally reaches the well-defined parabola profile on the larger scale. In particular, there is a "constricted" structure at $\sim35\,R_s$ (projected) from the core, where the jet cross section is locally shrinking. We suggest that an external pressure support/contribution from the inner part of accretion flow (presumably an ADAF-type hot accretion flow or associated corona) may be dynamically significant in shaping and confining the M87 jet on this scale.

3. Complementing our 86 GHz data with close-in-time multi-epoch lower-frequency data, we detected proper motions in both the main jet and the counter jet, which were all subrelativistic. The mean speed of the main jet components was $\beta_{app} \sim 0.32$, while the counter jet was slightly slower at $\beta_{app} \sim 0.17$. Comparing the measured proper motions in the jet and the counter jet, the viewing angle for the inner jet is estimated to be $\theta \sim 29°$–$45°$, although more dedicated studies of proper motion are necessary.

4. We reported on the first VLBI 86 GHz polarimetric result of the M87 jet. While it is still challenging to reveal the entire polarimetric property of this jet, we detected some polarized features near the jet base at this frequency. The detection of the polarization signals at this frequency implies that the magnitude of the RM toward these features is no larger than $\sim(5$–$17) \times 10^4$ rad m$^{-2}$, which is consistent with the result reported in the recent 230 GHz polarimetric study. Moreover, one of the polarized features has an observed fractional polarization up to $\sim20\%$, which is the highest value ever seen on pc-to-subpc scales of this jet. This indicates the presence of a well-ordered magnetic field in the formation and collimation zone of the M87 jet.

## APPENDIX
## THE CALIBRATOR 3C 273

Here we describe our data analysis and imaging for the bright quasar 3C 273 obtained by the 86 GHz VLBA+GBT program plus an additional 43 GHz archival data set. Checking the total-intensity and polarimetric status of this source is important for validating the results for M87 (particularly the polarimetric one).

3C 273 was observed on 2014 February 11 and 26 with VLBA+GBT at 86 GHz as an overall calibrator of our program. In the top-left panel of Figure 11 we show an 86 GHz total intensity image of 3C 273 taken on February 26. The observed jet structure consists of the bright core with several discrete knots down the jet. We achieved a dynamic range of 670 to 1, allowing a firm detection of the weaker emission down to $\sim5$ mas from the core. For comparison, in the top-right panel of Figure 11 we show a close-in-time VLBA 43 GHz image of this source that was observed on 2014 February 25 as a part of the Boston University blazar monitoring program. The dynamic range of the 86 GHz image is about twice that of the 43 GHz one. This enables a comparison of the images at a high confidence level, despite the steep-spectral nature of the synchrotron emission. The overall jet structure and the positions of the individual features in these two images are in excellent agreement with each other.

Regarding polarimetry, our results are summarized in the bottom two panels of Figure 11. The bottom-left panel shows the result obtained from the VLBA+GBT 86 GHz observation on 2014 February 26, while the bottom-right panel is the result from the VLBA 43 GHz observation on 2014 February 25. Within the central 2 mas of the jet, we identified three prominent polarized components that were consistently detected in the 86 and 43 GHz images. As described in Figure 11 these are termed P1, P2, and P3 starting from the upstream side. The highest polarized intensity at 43 GHz is in P2, while P1 is the strongest polarized component at 86 GHz. At both frequencies the largest fractional polarization was in P3 (10%–15%), while P1 was the smallest (4%–7%). The observed positions of P2 and P3 are in good agreement in both 43 and 86 GHz images. For the innermost component P1, the peak position of the polarized flux is slightly offset between 43 and 86 GHz, in the sense that the polarized emission at 86 GHz can be seen closer to the core than at 43 GHz. As described below, this is presumably due to the decrease in the Faraday depolarization effect at the higher frequency.

In terms of EVPA, we made use of the 43 GHz polarization image as a reference for our EVPA correction for the 86 GHz data. Here we assumed that the EVPA of the outermost component P3 is stable in both time and frequency, and performed a nominal EVPA correction by matching the observed 86 GHz EVPA of P3 to the 43 GHz one. The EVPA map shown in the bottom-left panel of Figure 11 was produced through this procedure. As a result, one can see that the EVPA of P2 is also closely aligned between the two frequencies. This indicates that the absolute difference in RM between P3 and P2 is relatively small.

On the other hand, the previous concurrent 43/86 GHz polarimetric VLBA study of this source suggested a large RM ($\sim2 \times 10^4$ rad m$^{-2}$) for the inner jet at $\sim0.8$ mas from the core (Attridge et al. 2005). In fact, examining our innermost component P1, we can find a notable difference in EVPA direction between the two frequencies, in contrast to the good
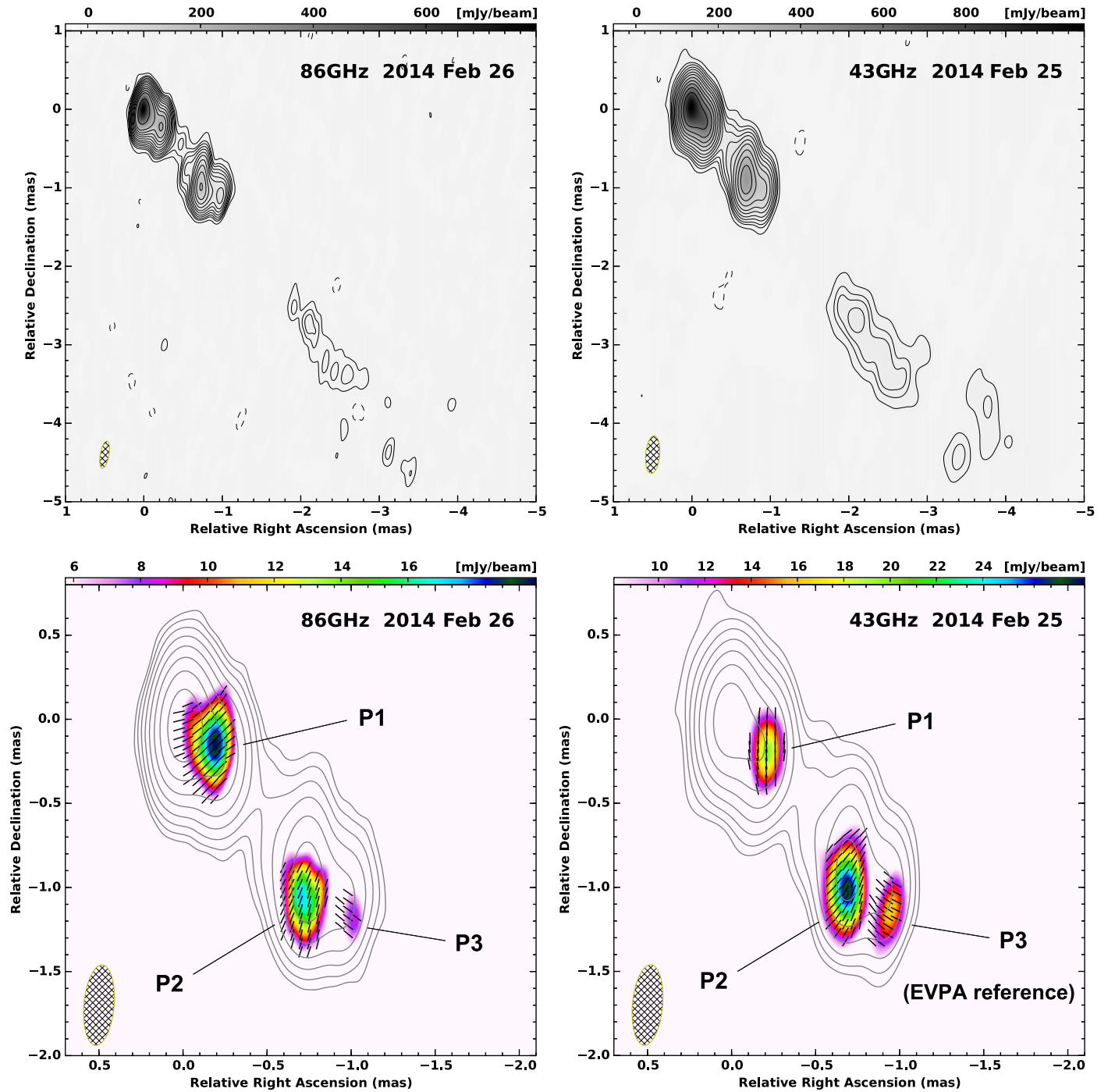
**Figure 11.** Total intensity and polarization images of 3C 273 at 86 and 43 GHz. The top-left panel is a VLBA+GBT 86 GHz total-intensity contour image observed on 2014 February 26. The beam size and the peak intensity are $0.34 \times 0.11$ mas at PA $-10°$ and 805 mJy beam$^{-1}$, respectively. The top-right panel is a 43 GHz VLBA total-intensity contour image observed on 2014 February 25. The beam size and the peak intensity are $0.48 \times 0.18$ mas at PA $-5°$ and 1100 mJy beam$^{-1}$, respectively. The bottom-left and the bottom-right panels are a close-up view of the inner jet at 86 and 43 GHz, respectively. In the bottom two panels, the images are restored with a common beam of $0.48 \times 0.18$ mas at PA $-5°$, corresponding to the synthesized beam of the 43 GHz data. The color map, the vectors, and the contours indicate the observed polarized intensity, the observed EVPA, and the total intensity distribution, respectively. P1, P2, and P3 indicate the polarized components that are consistently identified in both images. For the upper panels contours start from $-1$, 1, 2, $2^{3/2}$, 4, $2^{5/2}$... times $3\sigma$ rms level of each image ($1\sigma = 1.2$ mJy beam$^{-1}$ and 3.3 mJy beam$^{-1}$ at 86 and 43 GHz, respectively), while for the bottom panels contours are 1, 2, 4, 8... times 3.6 mJy beam$^{-1}$ and 9.9 mJy beam$^{-1}$ at 86 and 43 GHz, respectively.

EVPA alignment at P2 and P3. The observed EVPA difference in P1 between 43/86 GHz (with the assumption that the EVPAs of P3 are aligned between the two frequencies) is $\Delta\chi = \chi_{7\,\mathrm{mm}} - \chi_{3.5\,\mathrm{mm}} = 50°$. This indicates that there is an absolute difference in RM between P3 and P1 of at least

$|\mathrm{RM}| = 2.4 \times 10^4$ rad m$^{-2}$. This level of RM is very similar to that reported by Attridge et al. (2005). It seems that there is an additional (i.e., another $\sim15°$) rotation of EVPA at the near-core side of P1 in the 86 GHz image. This implies a further increase of RM toward the core, which is consistent with the

non-detection of a polarized signal in the corresponding region at 43 GHz.

To estimate the absolute uncertainty of our EVPA correction procedure, it is necessary to know the absolute difference in the EVPA of P3 between 43 and 86 GHz. Unfortunately this is difficult to derive from the present data alone. If P3 has a similar level of RM as seen toward P1, the EVPA distribution shown in the bottom-left panel of Figure 11 will have another $\sim 50°$ rotation. However, this level of uncertainty should be regarded as an upper limit, and the actual uncertainty should be smaller than this value, since P3 is located further downstream and shows a higher fractional polarization than P1, favoring a smaller amount of Faraday screen toward P3. On the larger scales (i.e., from a few to 10 mas from the core), several authors have reported RM values of hundreds to a few thousand rad m$^{-2}$ (e.g., Asada et al. 2002; Zavala & Taylor 2005). Looking at the adjacent component P2, there is actually a slight ($\sim 8°$) difference in EVPA between 43 and 86 GHz. This suggests an absolute difference in |RM| between P3 and P2 of $3.9 \times 10^3$ rad m$^{-2}$, which is just in between the values for P1 and the outer jet in the literature. Therefore, we consider that a level of $\sim 4 \times 10^3$ rad m$^{-2}$ would be a reasonable measure of |RM| at P3, and thus a likely uncertainty of our 86 GHz EVPA correction relative to the 43 GHz data would be $\Delta\chi_{RM} \sim 8°$. In summary, taking the EVPA uncertainty of the Boston 43 GHz map to be $\Delta\chi_{43\,GHz} \sim 10°$ (Jorstad et al. 2005), we estimate that a potential total uncertainty of EVPA in our 86 GHz images of 3C 273 is a level of $\Delta\chi_{3C273} \sim \Delta\chi_{43\,GHz} + \Delta\chi_{RM} \sim \pm 18°$.

## REFERENCES

Abramowski, A., Acero, F., Aharonian, F., et al. 2012, ApJ, 746, 151
Acciari, V. A., Aliu, E., Arlen, T., et al. 2009, Sci, 325, 444
Agudo, I., Bach, U., Krichbaum, T. P., et al. 2007, A&A, 476, L17
Aharonian, F., Akhperjanian, A. G., Bazer-Bachi, A. R., et al. 2006, Sci, 314, 1424
Akiyama, K., Lu, R.-S., Fish, V. L., et al. 2015, ApJ, 807, 150
Asada, K., Inoue, M., Uchida, Y., et al. 2002, PASJ, 54, L39
Asada, N., & Nakamura, M. 2012, ApJL, 745, L28
Attridge, J. M., Wardle, J. F. C., & Homan, D. C. 2005, ApJ, 633, 85
Begelman, M. C. 1998, ApJ, 493, 291
Begelman, M. C., Blandford, R. D., & Rees, M. J. 1984, RvMP, 56, 255
Biretta, J. A., Junor, W., & Livio, M. 2002, NewAR, 46, 239
Biretta, J. A., Sparks, W. B., & Macchetto, F. 1999, ApJ, 520, 621
Blakeslee, J. P., Jordán, A., Mei, S., et al. 2009, ApJ, 694, 556
Blandford, R. D., & Begelman, M. C. 1999, MNRAS, 303, L1
Blandford, R. D., & Payne, D. G. 1982, MNRAS, 199, 883
Blandford, R. D., & Rees, M. J. 1974, MNRAS, 169, 395
Blandford, R. D., & Znajek, R. L. 1977, MNRAS, 179, 433
Broderick, A. E., & Loeb, A. 2009, ApJ, 697, 1164
Burn, B. J. 1966, MNRAS, 133, 67
Casadio, C., Gomez, J.-L., Gandi, P., et al. 2015, ApJ, 808, 162
Chen, Y. J., Zhao, G.-Y., & Shen, Z.-Q. 2011, MNRAS, 416, L109
Clausen-Brown, E., Lyutikov, M., & Kharb, P. 2011, MNRAS, 415, 2081
Curtis, H. D. 1918, PLicO, 13, 9
Daly, R. A., & Marscher, A. P. 1988, ApJ, 334, 539
Deller, A. T., Brisken, W. F., Phillips, C. J., et al. 2011, PASP, 123, 275
Di Matteo, T., Allen, S. W., Fabien, A. C., & Wilson, A. S. 2003, ApJ, 582, 133
Dodson, R., Edwards, P. G., & Hirabayashi, H. 2012, PASJ, 58, 243
Doeleman, S. S., Fish, V. L., Schenck, D. E., et al. 2012, Sci, 338, 355
Fish, V., Alef, W., Anderson, J., et al. 2013, arXiv:1309.3519
Fomalont, E. B. 1999, in ASP Conf. Ser. 180, Synthesis Imaging in Radio Astronomy II, A Collection of Lectures from the Sixth NRAO/NMIMT Synthesis Imaging Summer School, ed. G. B. Taylor, C,L. Carilli, & R. A. Perley (ASP: San Francisco, CA), 301
Ford, H. C., Harms, R. J., Tsvetanov, Z. I., et al. 1994, ApJ, 435, 27
Gebhardt, K., Adams, J., Richstone, D., Lauer, T. R., & Faber, S. M. 2011, ApJ, 729, 119

Gebhardt, K., & Thomas, J. 2009, ApJ, 700, 1690
Ghisellini, G., Tavecchio, F., & Chiaberge, M. 2005, A&A, 432, 401
Giannios, D., Uzdensky, D. A., & Begelman, M. C. 2010, MNRAS, 402, 1649
Giroletti, M., Giovannini, G., Cotton, W. D., et al. 2008, A&A, 488, 905
Giroletti, M., Hada, K., Giovannini, G., et al. 2012, A&A, 538, L10
Gómez, J.-L., Marscher, A. P., Alberdi, A., Jorstad, S. G., & Agudo, I. 2001, ApJL, 561, L161
Gómez, J.-L., Marscher, A. P., Alberdi, A., Jorstad, S. G., & García-Miró, C. 2000, Sci, 289, 2317
Gómez, J.-L., Martí, J. M., Marscher, A. P., Ibáñez, J. M., & Alberdi, A. 1997, ApJL, 482, L33
Gopal-Krishna, Dhurde, S., Sircar, P., et al. 2007, MNRAS, 377, 446
Hada, K., Doi, A., Kino, M., et al. 2011, Natur, 477, 185 (H11)
Hada, K., Giroletti, M., Giovannini, G., et al. 2015, in 12th European VLBI Network Symposium and Users Mtg., Continuing EVN Monitoring of HST-1 in the Jet of M87, ed. A. Tarchi, M. Giroletti, & L. Feretti (Trieste: PoS), 18
Hada, K., Giroletti, M., Kino, M., et al. 2014, ApJ, 788, 165
Hada, K., Kino, M., Doi, A., et al. 2013, ApJ, 775, 70
Hada, K., Kino, M., Nagai, H., et al. 2012, ApJ, 760, 52
Harms, R. J., Ford, H. C., Tsvetanov, Z. I., et al. 1994, ApJ, 435, 35
Harris, D. E., Cheung, C. C., Biretta, J. A., et al. 2006, ApJ, 640, 211
Hirabayashi, H., Hirosawa, H., Kobayashi, H., et al. 1998, Sci, 281, 1825
Hodgson, J. A., Krichbaum, T. P., Marscher, A. P., et al. 2015, in 12th European VLBI Network Symposium and Users Mtg., Continuing EVN Monitoring of HST-1 in the Jet of M87, ed. A. Tarchi, M. Giroletti, & L. Feretti (Trieste: PoS), 28
Honma, M., Akiyama, K., Uemura, M., & Ikeda, S. 2014, PASJ, 66, 95
Hughes, D., Jáuregui Correa, J.-C., Schloerb, F. P., et al. 2010, Proc. SPIE, 7733, 31
Jorstad, S. G., Marscher, A. P., Lister, M. L., et al. 2005, AJ, 130, 1418
Junor, W., Biretta, J. A., & Livio, M. 1999, Natur, 401, 891
Junor, W., Biretta, J. A., & Wardle, J. F. C. 2001, in IAU Symp. 205, Galaxies and their Constituents at the Highest Angular Resolutions, ed. R. T. Schilizzi (ASP: San Francisco, CA), 136
Kardashev, N. S., Khartov, V. V., Abramov, V. V., et al. 2013, ARep, 57, 153
Kino, M., Takahara, F., Hada, K., et al. 2015, ApJ, 803, 30
Kino, M., Takahara, F., Hada, K., & Doi, A. 2014, ApJ, 786, 5
Kohler, S., Begelman, M. C., & Beckwith, K. 2012, MNRAS, 422, 2282
Komissarov, S. S., Barkov, M. V., Vlahakis, N., & Königl, A. 2007, MNRAS, 380, 51
Komissarov, S. S., & Falle, S. A. E. G. 1997, MNRAS, 288, 833
Komissarov, S. S., Vlahakis, N., Königl, A., & Barkov, M. V. 2009, MNRAS, 394, 1182
Königl, A. 1981, ApJ, 243, 700
Kovalev, Y. Y., Lister, M. L., Homan, D. C., & Kellermann, K. I. 2007, ApJL, 668, L27
Koyama, S., Kino, M., Giroletti, M., et al. 2015, in 12th European VLBI Network Symposium and Users Mtg., Continuing EVN Monitoring of HST-1 in the Jet of M87, ed. A. Tarchi, M. Giroletti, & L. Feretti (Trieste: PoS), 91
Krichbaum, T. P., Graham, D. A., Bremer, M., et al. 2006, JPhCS, 54, 328
Kuo, C. Y., Asada, K., Rao, R., et al. 2014, ApJL, 783, L33
Laing, R. A. 1980, MNRAS, 193, 439
Lee, S.-S., Lobanov, A. P., Krichbaum, T. P., et al. 2008, A&A, 136, 159
Lenain, J.-P., Boisson, C., Sol, H., & Katarzyński, K. 2008, A&A, 478, 111
Leppänen, K. J., Zensus, J. A., & Diamond, P. J. 1995, AJ, 110, 2479
Lobanov, A. P., & Zensus, J. A. 2001, Sci, 294, 128
Ly, C., Walker, R. C., & Junor, W. 2007, ApJ, 660, 200
Ly, C., Walker, R. C., & Wrobel, J. M. 2004, AJ, 127, 119
Macchetto, F., Marconi, A., Axon, D. J., et al. 1997, ApJ, 489, 579
Martí-Vidal, I., Krichbaum, T. P., Marscher, A., et al. 2012, A&A, 542, A107
Matsumoto, J., Masada, Y., & Shibata, K. 2012, ApJ, 751, 140
McKinney, J. C. 2006, MNRAS, 368, 1561
McKinney, J. C., & Blandford, R. 2009, MNRAS, 394, L126
McKinney, J. C., & Narayan, R. 2007, MNRAS, 375, 513
McKinney, J. C., Tchekhovskoy, A., & Blandford, R. 2012, MNRAS, 423, 3083
Mizuno, Y., Gomez, J.-L., Nishikawa, K., et al. 2015, ApJ, 809, 38
Molina, S. N., Agudo, I., Gómez, J. L., et al. 2014, A&A, 566, 26
Morsony, B. J., Lazzati, D., & Begelman, M. C. 2007, ApJ, 665, 569
Nagai, H., Haga, T., Giovannini, G., et al. 2014, ApJ, 785, 53
Nakamura, M., & Asada, K. 2013, ApJ, 775, 118
Nakamura, M., Li, H., & Li, S. 2006, ApJ, 652, 1059
Narayan, R., & Yi, I. 1994, ApJL, 428, L13

Narayan, R., & Yi, I. 1995, ApJ, 444, 231
Owen, F. N., Hardee, P. E., & Cornwell, T. J. 1989, ApJ, 340, 698
Perlman, E. S., Adams, S. C., Cara, M., et al. 2011, ApJ, 743, 119
Perlman, E. S., Biretta, J. A., Sparks, W. B., Macchetto, F. D., & Leahy, J. P. 2001, ApJ, 551, 206
Perlman, E. S., Biretta, J. A., Zhou, F., Sparks, W. B., & Macchetto, F. D. 1999, AJ, 117, 2185
Quataert, E., & Gruzinov, A. 2000, ApJ, 539, 809
Reynolds, C. S., Fabian, A. C., Celotti, A., & Rees, M. J. 1996, MNRAS, 283, 873
Rioja, M., & Dodson, R. 2011, AJ, 141, 114
Roberts, D. H., Wardle, J. F. C., & Brown, L. F. 1994, ApJ, 427, 718

Shepherd, M. C., Pearson, T. J., & Taylor, G. B. 1994, BAAS, 26, 987
Stawarz, Ł., & Ostrowski, M. 2002, ApJ, 578, 763
Tchekhovskoy, A., Narayan, R., & McKinney, J. C. 2011, MNRAS, 418, L79
Walker, R. C., Ly, C., Junor, W., & Hardee, P. J. 2008, JPhCS, 131, 012053
Walsh, J. L., Barth, A. J., Ho, L. C., & Sarzi, M. 2013, ApJ, 770, 86
Yuan, F., & Narayan, R. 2014, ARA&A, 52, 529
Yuan, F., Wu, M., & Bu, D. 2012, ApJ, 761, 129
Zakamska, N. L., Begelman, M. C., & Blandford, R. D. 2008, ApJ, 679, 990
Zavala, R. T., & Taylor, G. B. 2002, ApJL, 566, L9
Zavala, R. T., & Taylor, G. B. 2005, ApJL, 626, L73